Performance of the CMS muon detector and muon reconstruction with proton-proton collisions at $\sqrt{s}$=13 TeV

Published by IOP Publishing for Sissa Medialab

Received: *April 12, 2018*
Accepted: *June 7, 2018*
Published: *June 19, 2018*

Performance of the CMS muon detector and muon reconstruction with proton-proton collisions at $\sqrt{s} = 13$ TeV

The CMS collaboration

E-mail: cms-publication-committee-chair@cern.ch

Abstract: The CMS muon detector system, muon reconstruction software, and high-level trigger underwent significant changes in 2013–2014 in preparation for running at higher LHC collision energy and instantaneous luminosity. The performance of the modified system is studied using proton-proton collision data at center-of-mass energy $\sqrt{s} = 13$ TeV, collected at the LHC in 2015 and 2016. The measured performance parameters, including spatial resolution, efficiency, and timing, are found to meet all design specifications and are well reproduced by simulation. Despite the more challenging running conditions, the modified muon system is found to perform as well as, and in many aspects better than, previously. We dedicate this paper to the memory of Prof. Alberto Benvenuti, whose work was fundamental for the CMS muon detector.

Keywords: Muon spectrometers; Particle tracking detectors (Gaseous detectors)

ArXiv ePrint: 1804.04528

https://doi.org/10.1088/1748-0221/13/06/P06015

2018 JINST 13 P06015

Contents

1 Introduction **1**

2 Muon detectors **2**

3 Muon reconstruction **6**
- 3.1 Hit and segment reconstruction 6
- 3.2 Muon track reconstruction 8
- 3.3 Muon identification 9
- 3.4 Determination of muon momentum 10
- 3.5 Muon isolation 11

4 Data and simulated samples **12**

5 Spatial resolution **12**

6 Efficiency **16**
- 6.1 Hit and segment efficiency 16
- 6.2 Reconstruction, identification and isolation efficiency 18

7 Momentum scale and resolution **21**
- 7.1 Low and intermediate p_T: scale and resolution with collisions 21
- 7.2 Momentum resolution with cosmic rays 22
- 7.3 High p_T: momentum scale with collisions 23

8 Timing **24**

9 Trigger **26**
- 9.1 Trigger primitives 28
- 9.2 Trigger efficiencies and rates 30

10 Summary **33**

The CMS collaboration **38**

2018 JINST 13 P06015

1 Introduction

The Compact Muon Solenoid (CMS) detector at the CERN LHC is a general purpose device designed primarily to search for signatures of new physics in proton-proton (pp) and heavy ion (proton-ion and ion-ion) collisions. Since many of these signatures include muons, CMS is constructed with

subdetectors to identify muons, trigger the CMS readout upon their detection, and measure their momentum and charge over a broad range of kinematic parameters. In this paper, the composite whole of muon subdetectors is called the muon detector, and the software algorithms used to combine the data from all CMS subdetectors to characterize the physics objects created in collisions are collectively referred to as particle reconstruction. Previous published studies of the performance of the CMS muon detector [1] and muon reconstruction [2] were based on data from pp collisions at center-of-mass energy $\sqrt{s} = 7$ TeV. These data were collected in 2010, the first full year of LHC operations (the first year of "Run 1", which lasted from 2010 to 2012). To prepare for the higher collision energy and luminosity of the subsequent running period ("Run 2", beginning in 2015), significant improvements were made to the muon system in 2013–2014 during the long shutdown period between Runs 1 and 2. These improvements will be described in section 2. The present paper describes the performance of the Run 2 CMS muon system, and covers the subdetectors, the reconstruction software, and the high-level trigger. It is based on data collected in 2015 and 2016 from pp collisions at $\sqrt{s} = 13$ TeV with instantaneous luminosities up to 8×10^{33} cm^{-2} s^{-1}. As a result of these improvements to the muon detector and reconstruction algorithms, and in spite of the higher instantaneous luminosity, the performance of the muon detector and reconstruction is as good as or better than in 2010. Moreover, all performance parameters remain well within the design specifications of the CMS muon detector [3].

An extensive description of the performance of the muon detector and the muon reconstruction software has been given in ref. [1] and ref. [2]. Therefore, in this paper, representative performance plots from individual muon subsystems are shown and results from the other subsystems, when pertinent, are described in the text. A description of the different subdetectors forming the CMS muon detector is given in section 2. The muon reconstruction, identification, and isolation algorithms are outlined in section 3, followed by a short description of the data and simulation samples used in section 4. The performance of individual muon subdetectors and that of the full system is described in detail, particularly with regard to spatial resolution (section 5), efficiency (section 6), momentum scale and resolution (section 7), and timing (section 8). The design and performance of the high-level trigger is described in section 9. The results are summarized in section 10.

2 Muon detectors

A detailed description of the CMS detector, together with a definition of the coordinate system and the relevant kinematic variables, can be found in ref. [4]. A schematic diagram of the CMS detector is shown in figure 1. The CMS detector has a cylindrical geometry that is azimuthally (ϕ) symmetric with respect to the beamline and features a superconducting magnet, which provides a 3.8 T solenoidal field oriented along the beamline. An inner tracker comprising a silicon pixel detector and a silicon strip tracker is used to measure the momentum of charged particles in the pseudorapidity range $|\eta| < 2.5$. The muon system is located outside the solenoid and covers the range $|\eta| < 2.4$. It is composed of gaseous detectors sandwiched among the layers of the steel flux-return yoke that allow a traversing muon to be detected at multiple points along the track path.

Three types of gas ionization chambers were chosen to make up the CMS muon system: drift tube chambers (DTs), cathode strip chambers (CSCs), and resistive plate chambers (RPCs). A detailed description of these chambers, including gas composition and operating voltage, can be found in ref. [1]. The DTs are segmented into drift cells; the position of the muon is determined by

2018 JINST 13 P06015

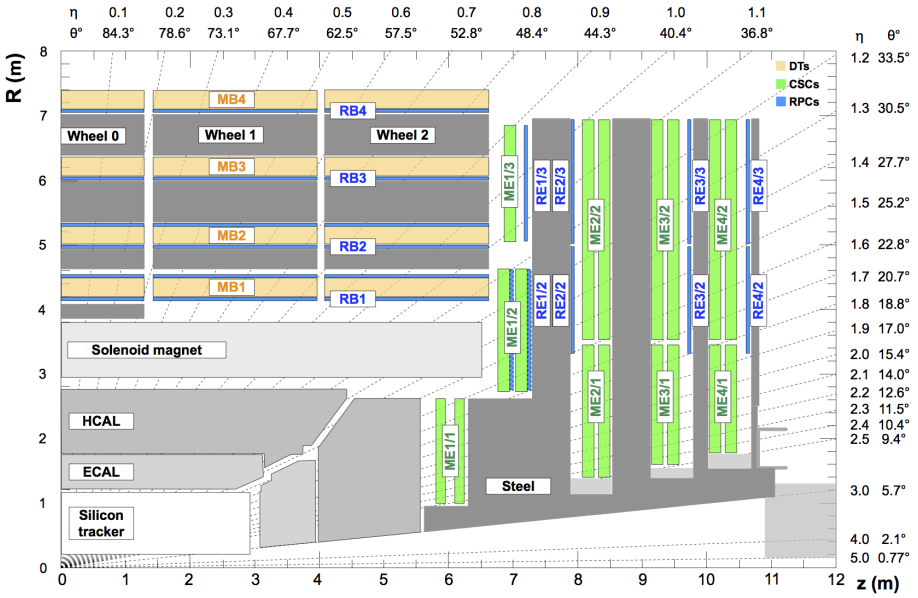

Figure 1. An R-z cross section of a quadrant of the CMS detector with the axis parallel to the beam (z) running horizontally and the radius (R) increasing upward. The interaction point is at the lower left corner. The locations of the various muon stations and the steel flux-return disks (dark areas) are shown. The drift tube stations (DTs) are labeled MB ("Muon Barrel") and the cathode strip chambers (CSCs) are labeled ME ("Muon Endcap"). Resistive plate chambers (RPCs) are mounted in both the barrel and endcaps of CMS, where they are labeled RB and RE, respectively.

measuring the drift time to an anode wire of a cell with a shaped electric field. The CSCs operate as standard multi-wire proportional counters but add a finely segmented cathode strip readout, which yields an accurate measurement of the position of the bending plane (R-ϕ) coordinate at which the muon crosses the gas volume. The RPCs are double-gap chambers operated in avalanche mode and are primarily designed to provide timing information for the muon trigger. The DT and CSC chambers are located in the regions $|\eta| < 1.2$ and $0.9 < |\eta| < 2.4$, respectively, and are complemented by RPCs in the range $|\eta| < 1.9$. We distinguish three regions, naturally defined by the cylindrical geometry of CMS, referred to as the barrel ($|\eta| < 0.9$), overlap ($0.9 < ||\eta|| < 1.2$), and endcap ($1.2 < |\eta| < 2.4$) regions. The chambers are arranged to maximize the coverage and to provide some overlap where possible. An event in which two muons are reconstructed, one in the barrel and one in the endcap, is shown in figure 2.

In the barrel, a station is a ring of chambers assembled between two layers of the steel flux-return yoke at approximately the same value of radius R. There are four DT and four RPC stations in the barrel, labeled MB1–MB4 and RB1–RB4, respectively. Each DT chamber consists of three "superlayers", each comprising four staggered layers of parallel drift cells. The wires in each layer are oriented so that two of the superlayers measure the muon position in the bending plane (R-ϕ) and one superlayer measures the position in the longitudinal plane (R-θ). However, the chambers in MB4 have only the two R-ϕ superlayers. The two innermost RPC barrel stations, RB1 and RB2, are instrumented with two layers of RPCs each, facing the innermost and outermost sides of the DT. For stations 3 and 4 the RPCs have only one detection layer. The RPC strips are oriented parallel to the

2018 JINST 13 P06015

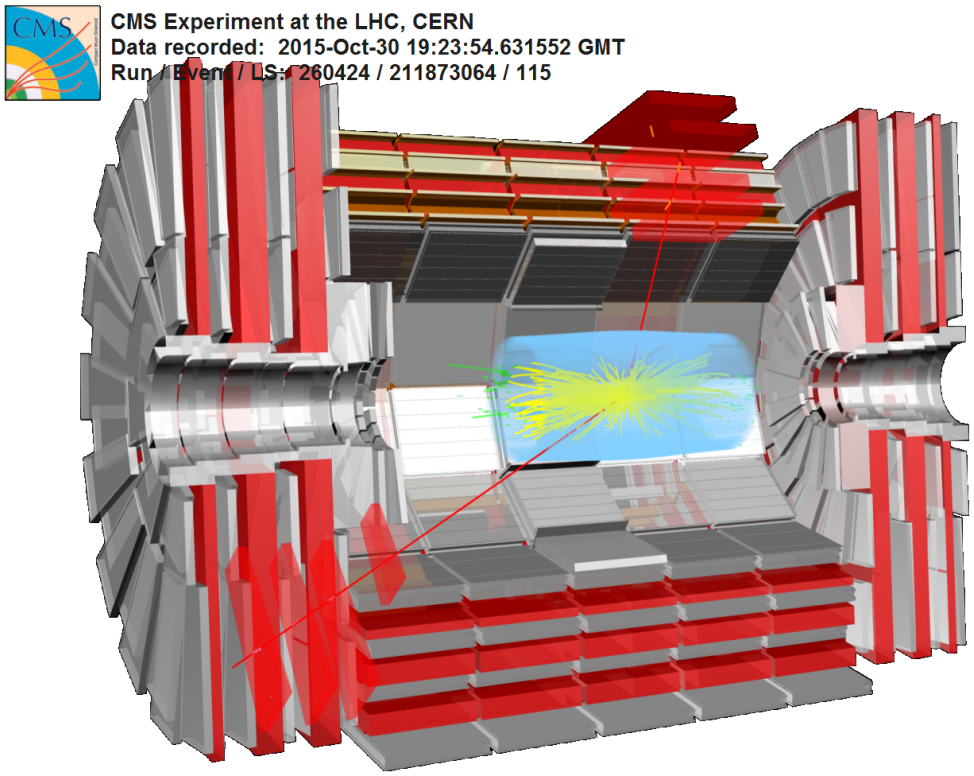

Figure 2. A pp collision event with two reconstructed muon tracks superimposed on a cutaway image of the CMS detector. The image has been rotated around the y axis, which makes the inner tracker appear offset relative to its true position in the center of the detector. The four layers of muon chambers are interleaved with three layers of the steel flux-return yoke. The reconstructed invariant mass of the muon pair is 2.4 TeV. One muon is reconstructed in the barrel with a transverse momentum (p_{T}) of 0.7 TeV, while the second muon is reconstructed in the endcap with p_{T} of 1.0 TeV.

wires of the DT chambers that measure the coordinate in the bending plane. From the readout point of view, every RPC is subdivided into two or three η partitions called "rolls" [5]. Both DT and RPC barrel stations are arranged in five "wheels" along the z dimension, with 12 ϕ-sectors per wheel.

In the endcap, a station is a ring of chambers assembled between two disks of the steel flux-return yoke at approximately the same value of z. There are four CSC and four RPC stations in each endcap, labeled ME1–ME4 and RE1–RE4, respectively. Between Run 1 and Run 2, additional chambers were added in ME4 and RE4 to increase redundancy, improve efficiency, and reduce misidentification rates. Each CSC chamber consists of six staggered layers, each of which measures the muon position in two coordinates. The cathode strips are oriented radially to measure the muon position in the bending plane (R-ϕ), whereas the anode wires provide a coarse measurement in R. The RPC strips are oriented parallel to the CSC strips to measure the coordinate in the bending plane, and each endcap chamber is divided into three $|\eta|$ partitions (rolls) identified by the letters A, B, and C. In the radial direction, stations are arranged in two or three "rings" of endcap RPCs and CSCs. In the inner rings of stations 2, 3, and 4, each CSC chamber subtends a ϕ angle of 20°; all other CSCs subtend an angle of 10°.

2018 JINST 13 P06015

Table 1. Properties and parameters of the CMS muon subsystems during the 2016 data collection period.

Muon subsystem	DT	CSC	RPC
$\lvert\eta\rvert$ coverage	0.0–1.2	0.9–2.4	0.0–1.9
Number of stations	4	4	4
Number of chambers	250	540	Barrel: 480 Endcap: 576
Number of layers/chamber	R-ϕ: 8; z: 4	6	2 in RB1 and RB2 1 elsewhere
Number of readout channels	172 000	Strips: 266 112 Anode channels: 210 816	Barrel: 68 136 Endcap: 55 296
Percentage of active channels	98.4%	99.0%	98.3%

Using these conventions, in this paper the performance of the DTs is specified according to chamber type, labeled "MBn±w", where n is the barrel station (increasing with R), + or − specifies the z-direction, and w is the wheel (increasing with $|z|$, with w = 0 centered at $z = 0$). The CSCs are labeled "ME±n/m", where + or − specifies the z-direction, n is the endcap station (increasing with $|z|$), and m is the ring (increasing with R). If no sign is specified, the performance of the + and − stations are combined. The inner ring of the CSC chambers in station 1 has a structure that is different from the other rings; the primary difference is an additional division of ME1/1 into two η partitions called a and b [1]. An overview of the number of chambers per chamber type, number of readout channels, and number of active channels in 2016 is given in table 1.

The CMS trigger system consists of two stages [6] and is described in more detail in section 9. A level-1 (L1) trigger based on custom-made electronics reduces the event rate from 40 MHz (LHC bunch crossing rate) to a readout rate of 100 kHz. For the muon component of the L1 trigger, CSC and DT chambers provide "trigger primitives" constructed from hit patterns consistent with muons that originate from the collision region, and RPC chambers provide hit information. When a specific bunch crossing is selected by the L1 algorithms as a potential event, readout of the precision data from the CMS detector is initiated via the "L1-Accept" (L1A) signal, which is synchronously distributed to all CMS subsystems. The high-level trigger (HLT), based on a farm of microprocessors, uses the precision data to reconstruct events to further reduce the rate of data to preserve for offline analysis to approximately 1 kHz. Both L1 and HLT use information from the muon system to efficiently identify muons over the broad energy range required for physics signatures of interest while minimizing the trigger rate and operating within the available latency.

The LHC is a bunched machine, in which the accelerated protons are distributed in bunches separated by one or more time steps of 25 ns. The running conditions of the LHC have evolved continuously since the beginning of its operation, and are expected to continue to evolve in the future [7–9]. As a representative comparison, we compare the LHC conditions in fill 1440 (October 2010), included in the dataset analyzed in refs. [1, 2], with the conditions in fill 5013 (June 2016), included in the 2016 data used in this paper. Between these two fills, the center-of-mass energy

2018 JINST 13 P06015

increased from $\sqrt{s} = 7$ TeV to $\sqrt{s} = 13$ TeV. The maximum instantaneous luminosity increased by about a factor of 40, from $2{\times}10^{32}$ cm^{-2} s^{-1} to $8{\times}10^{33}$ cm^{-2} s^{-1}, as a result of the increases in both the number of colliding bunches and the luminosity per bunch. The number of colliding bunches increased by about a factor of 6, from 348 to 2028, facilitated by the reduction of the spacing between proton bunches from 150 ns to 25 ns. The average luminosity per bunch increased by about a factor of 6.5, from $0.6{\times}10^{30}$ cm^{-2} s^{-1} to $3.9{\times}10^{30}$ cm^{-2} s^{-1}, as a result of several changes including increasing the number of protons per bunch, reducing the transverse widths of the beams, and focusing the beams more tightly [8, 9]. The combined increases in collision energy and luminosity per bunch caused the average number of inelastic collisions per crossing (pileup) to increase by about a factor of 8, from 3.6 to 28.

In order to prepare for these challenging LHC conditions and to exploit the corresponding gain in luminosity, the CMS muon system was significantly modified between Run 1 and Run 2. As mentioned previously, additional RPC and CSC chambers, RE4 and ME4/2, were installed in the fourth station to increase redundancy, improve efficiency, and reduce misidentification rates. The trigger and readout electronics were improved as part of the CMS-wide trigger upgrade [10], including optical links in the DTs and CSCs to increase bandwidth and to ease maintenance [11, 12]. New electronics were installed in the CSC ME1/1 chambers to read out every strip in the ME1/1a ring, covering $2.1 < |\eta| < 2.4$. These strips had been ganged together in Run 1, combining every 16th strip, which led to a 3-fold ambiguity for the position of a hit on that strip plane. The removal of the strip ganging in Run 2 leads to reduced capacitance, in turn leading to reduced noise and a resulting improvement in the ϕ resolution in ME1/1a.

3 Muon reconstruction

3.1 Hit and segment reconstruction

This section gives a brief overview of the "local" reconstruction algorithms in the CMS muon detector. Local reconstruction uses information from only a single muon chamber (RPC, CSC, or DT) to specify the passage of a muon through the chamber [1].

Muons and other charged particles that traverse a muon subdetector ionize the gas in the chambers, which eventually causes electric signals to be produced on the wires and strips. These signals are read out by electronics and are associated with well-defined locations, generically called "hits", in the detector. The precise location of each hit is reconstructed from the electronic signals using different algorithms depending on the detector technology.

Hit reconstruction in a DT drift cell specifies the transverse distance between the wire and the intersection of the muon trajectory with the plane containing the wires in the layer. The electrons produced through gas ionization by a muon crossing the cell are collected at the anode wire. A time-to-digital converter (TDC) registers their arrival time, T_{TDC}. This time is then corrected by a time pedestal, T_{ped}, and multiplied by the electron drift velocity, v, to reconstruct the position of the DT hit:

$$\text{position} = (T_{\mathrm{TDC}} - T_{\mathrm{ped}}) \times v. \tag{3.1}$$

The DT drift cell was designed to provide a uniform electric field so that the drift velocity can be assumed to be mostly constant for tracks impinging on the cell perpendicular to the plane of wires.

2018 JINST 13 P06015

The effect of deviations from this assumption on the spatial resolution is described in section 5. In equation (3.1), the time pedestal accounts for the time from the bunch crossing until the trigger decision arrives at the chamber electronics. It includes the time-of-flight (at the speed of light) along a straight line from the interaction region to the center of the wire, the average signal propagation time along the wire, the generation of trigger primitives, the processing by the L1 trigger electronics, the distribution of the L1A signals, and the receipt of L1A back at the readout electronics on the chamber. It also includes a wire-by-wire component that takes into account the different signal paths within a chamber. In another iteration, the time-of-flight and signal propagation time are refined using the segment position from the orthogonal superlayer available for MB1, MB2, and MB3. The calibration of T_{ped} and v is described in detail in ref. [1]. Effectively, the drift time is tuned to make $(T_{\text{TDC}} - T_{\text{ped}}) = 0$ for muons that cross the chamber at the location of the wire.

Hit reconstruction in a CSC layer measures the position of the traversing muon by combining information from the cathode strips and anode wires. The strips are radial, each subtending an angle of about 3 mrad (different chamber types have different angular strip widths that range from 2.2 to 4.7 mrad) and can thus accurately measure the ϕ angle. This is the bending direction of a muon traveling through the endcaps. In the endcaps the solenoidal field is first parallel to the z direction but then diverges radially, so a muon is first deflected in one azimuthal direction and then deflected in the opposite direction, with the maximum deflection occurring in the first station. The wires are orthogonal to the strips, except in ME1/1 where they are tilted to compensate for the Lorentz drift of ionization electrons in the non-negligible magnetic field in this region. They are ganged into wire groups of about 1–2 cm width, which results in a coarser-grained measurement in the radial direction. A CSC hit is reconstructed at the intersection points of hit strips and wire groups. A CSC reconstructed hit also has a measured time, which is calibrated such that hits from muons produced promptly in the triggering bunch crossing have a time distribution centered around zero.

Hit reconstruction in an RPC chamber requires clustering of hit strips. A charged particle passing through the RPC produces an avalanche of electrons in the gap between two plates. This charge induces a signal on an external strip readout plane to identify muons from collision events with a precision of a few ns. The strips are aligned with η with up to 2 cm strip pitch, therefore giving a few cm spatial resolution in the ϕ coordinate. Since the ionization charge from a muon can be shared by more than one strip, adjacent strips are clustered to reconstruct one hit. An RPC hit is reconstructed as the strip cluster centroid.

While the RPC chambers are single-layer chambers, the CSC and DT chambers are multi-layer detectors where hits are reconstructed in each layer. From the reconstructed hits, straight-line track "segments" are built within each CSC or DT chamber.

Segment reconstruction in the DTs was modified prior to Run 2 [13]. The calibration of T_{ped} in eq. (3.1) implicitly assumes that all muons take the same time to reach the reconstructed hit position from the interaction region. However, this assumption is not exactly true since hits could come from muons originating from other bunch crossings ("out-of-time muons"), or could be produced by heavy particles that travel at a reduced speed. Any such shift in the muon crossing time would cause all hits produced within a chamber to be shifted in space by the same amount. Therefore, DT segment reconstruction was modified prior to Run 2 to include time as third parameter, in addition to the intercept and slope of the standard two-dimensional straight-line pattern recognition and fit algorithm (in the plane transverse to the wire direction). The inclusion of time into

2018 JINST 13 P06015

segment reconstruction allows spurious early hits, produced by delta rays, to be removed from the segment reconstruction and thus improves the spatial resolution (see section 5). The segment time information is not needed in the muon track reconstruction algorithm because of the negligible rate of accidentally matching out-of-time segments. The timing data are, however, kept with the reconstructed muon track information to be used in physics analyses (see section 8).

3.2 Muon track reconstruction

In the standard CMS reconstruction procedure for pp collisions [2, 14, 15], tracks are first reconstructed independently in the inner tracker (tracker track) and in the muon system (standalone-muon track), and then used as input for muon track reconstruction.

Tracker tracks are built using an iterative approach, running a sequence of tracking algorithms, each with slightly different logic. After each iteration step, hits that have been associated with reconstructed tracks are removed from the set of input hits to be used in the following step. This approach maintains high performance and reduces processing time [14].

Standalone-muon tracks are built by exploiting information from muon subdetectors to gather all CSC, DT, and RPC information along a muon trajectory using a Kalman-filter technique [16]. Reconstruction starts from seeds made up of groups of DT or CSC segments.

Tracker muon tracks are built "inside-out" by propagating tracker tracks to the muon system with loose matching to DT or CSC segments. Each tracker track with transverse momentum $p_{\mathrm{T}} > 0.5\,\mathrm{GeV}$ and a total momentum $p > 2.5\,\mathrm{GeV}$ is extrapolated to the muon system. If at least one muon segment matches the extrapolated track, the tracker track qualifies as a tracker muon track. The track-to-segment matching is performed in a local *(x,y)* coordinate system defined in a plane transverse to the beam axis, where x is the better-measured coordinate (in the R-ϕ plane) and y is the coordinate orthogonal to it. The extrapolated track and the segment are matched either if the absolute value of the difference between their positions in the x coordinate is smaller than 3 cm, or if the ratio of this distance to its uncertainty (pull) is smaller than 4.

Global muon tracks are built "outside-in" by matching standalone-muon tracks with tracker tracks. The matching is done by comparing parameters of the two tracks propagated onto a common surface. A combined fit is performed with the Kalman filter using information from both the tracker track and standalone-muon track.

Owing to the high efficiency of the tracker track and muon segment reconstruction, about 99% of the muons produced within the geometrical acceptance of the muon system are reconstructed either as a global muon track or as a tracker muon track, and very often as both. Global muons and tracker muons that share the same tracker track are merged into a single candidate.

Tracker muons have high efficiency in regions of the CMS detector with less instrumentation (for routing of detector services) and for muons with low p_{T}. The tracker muons that are not global muons typically match only to segments in the innermost muon station, but not other stations. This increases the probability of muon misidentification since hadron shower remnants can reach this innermost muon station (punch-through). Global muon reconstruction, which uses standalone-muon tracks, is designed to have high efficiency for muons penetrating through more than one muon station, which reduces the muon misidentification rate compared to tracker muons. By fully exploiting the information from both the inner tracker and the muon system, the p_{T} measurement of global muons is also improved compared to tracker muons, especially for $p_{\mathrm{T}} > 200\,\mathrm{GeV}$. Muons

2018 JINST 13 P06015

reconstructed only as standalone-muon tracks have worse momentum resolution and a higher admixture of cosmic muons than global or tracker muons.

Reconstructed muons are fed into the CMS particle flow (PF) algorithm [17]. The algorithm combines information from all CMS subdetectors to identify and reconstruct all individual particles for each event, including electrons, neutral hadrons, charged hadrons, and muons. For muons, PF applies a set of selection criteria to candidates reconstructed with the standalone, global, or tracker muon algorithms. The requirements are based on various quality parameters from the muon reconstruction (described in section 3.3), as well as make use of information from other CMS subdetectors (e.g., isolation as described in section 3.5).

Prior to Run 2, two muon-specific calculations were added to the tracker track reconstruction to keep reconstruction and identification efficiency as high as possible under high-pileup conditions [17]. In the first calculation, tracker tracks identified as tracker muons are rebuilt by relaxing some quality constraints to increase track hit efficiency. In the second, standalone-muon tracks with $p_{\mathrm{T}} > 10\,\mathrm{GeV}$ that fulfill a minimal set of quality requirements are used to seed an outside-in inner tracking reconstruction step. This additional set of tracks is combined with those provided by the inner tracking system and is exploited to build global and tracker muons.

3.3 Muon identification

A set of variables was studied and selection criteria were defined to allow each analysis to tune the desired balance between efficiency and purity. Some variables are based on muon reconstruction, such as track fit χ^2, the number of hits per track (either in the inner tracker or in the muon system, or both), or the degree of matching between tracker tracks and standalone-muon tracks (for global muons). The muon segment compatibility is computed by propagating the tracker track to the muon system, and evaluating both the number of matched segments in all stations and the closeness of the matching in position and direction [15]. The algorithm returns values in a range between 0 and 1, with 1 representing the highest degree of compatibility. A kink-finding algorithm splits the tracker track into two separate tracks at several places along the trajectory. For each split the algorithm makes a comparison between the two separate tracks, with a large χ^2 indicating that the two tracks are incompatible with being a single track. Other variables exploit inputs from outside the reconstructed muon track, such as compatibility with the primary vertex (the reconstructed vertex with the largest value of summed physics-object p_{T}^2 [18]). Using these variables, the main identification types of muons used in CMS physics analyses include:

- *Loose muon identification (ID)* aims to identify prompt muons originating at the primary vertex, and muons from light and heavy flavor decays, as well as maintain a low rate of the misidentification of charged hadrons as muons. A loose muon is a muon selected by the PF algorithm that is also either a tracker or a global muon.

- *Medium muon ID* is optimized for prompt muons and for muons from heavy flavor decay. A medium muon is a loose muon with a tracker track that uses hits from more than 80% of the inner tracker layers it traverses. If the muon is only reconstructed as a tracker muon, the muon segment compatibility must be greater than 0.451. If the muon is reconstructed as both a tracker muon and a global muon, the muon segment compatibility need only be greater than 0.303, but then the global fit is required to have goodness-of-fit per degree of freedom

2018 JINST 13 P06015

(χ^2/dof) less than 3, the position match between the tracker muon and standalone-muon must have $\chi^2 < 12$, and the maximum χ^2 computed by the kink-finding algorithm must be less than 20. The constraints on the segment compatibility were tuned after application of the other constraints to target an overall efficiency of 99.5% for muons from simulated W and Z events.

- *Tight muon ID* aims to suppress muons from decay in flight and from hadronic punch-through. A tight muon is a loose muon with a tracker track that uses hits from at least six layers of the inner tracker including at least one pixel hit. The muon must be reconstructed as both a tracker muon and a global muon. The tracker muon must have segment matching in at least two of the muon stations. The global muon fit must have χ^2/dof < 10 and include at least one hit from the muon system. A tight muon must be compatible with the primary vertex, having a transverse impact parameter $|dXY| < 0.2$ cm and a longitudinal impact parameter $|dz| < 0.5$ cm.

- *Soft muon ID* is optimized for low-p_T muons for B-physics and quarkonia analyses. A soft muon is a tracker muon with a tracker track that satisfies a high purity flag [14] and uses hits from at least six layers of the inner tracker including at least one pixel hit. The tracker muon reconstruction must have tight segment matching, having pulls less than 3 both in local x and in local y. A soft muon is loosely compatible with the primary vertex, having $|dXY| < 0.3$ cm and $|dz| < 20$ cm.

- *High momentum muon ID* is optimized for muons with $p_T > 200$ GeV. A high momentum muon is reconstructed as both a tracker muon and a global muon. The requirements on the tracker track, the tracker muon, and the transverse and longitudinal impact parameters are the same as for a tight muon, as well as the requirement that there be at least one hit from the muon system for the global muon. However, in contrast to the tight muon, the requirement on the global muon fit χ^2/dof is removed. The removal of the χ^2 requirement prevents inefficiencies at high p_T when muons radiate large electromagnetic showers as they pass through the steel flux-return yoke, giving rise to additional hits in the muon chambers. A requirement on the relative p_T uncertainty, $\sigma(p_T)/p_T < 30\%$, is used to ensure a proper momentum measurement.

3.4 Determination of muon momentum

The default algorithm used by CMS to determine the muon momentum is the *Tune-P* algorithm [2]. For each muon, the *Tune-P* algorithm selects the p_T measurement from one of the following refits based on goodness-of-fit information and $\sigma(p_T)/p_T$ criteria to reduce tails in the momentum resolution distribution due to poor quality fits.

- *Inner-Track fit* determines the momentum using only information from the inner tracker. While various fit methods are used to add information from the muon detector to improve the measurement of the momentum at high p_T, for muons with $p_T < 200$ GeV, the contribution from the muon system to the momentum measurement is marginal. Therefore, the inner-track fit is highly favored by *Tune-P* at low momentum.

- *Tracker-Plus-First-Muon-Station fit* starts with the hits from the global muon track and performs a refit using only information from the inner tracker and the innermost muon station

2018 JINST 13 P06015

containing hits. The innermost station provides the best information about momentum within the muon system.

- *Picky fit* aims at properly determining the momentum for events in which showering occurred within a chamber. This algorithm again starts with the hits from the global muon track, but in chambers that have a large hit occupancy (i.e. likely from a shower) the refit uses only the hits that are compatible with the extrapolated trajectory (based on χ^2).

- *Dynamic-Truncation fit* accounts for cases when energy losses cause significant bending of the muon trajectory. The algorithm propagates the tracker track to the innermost station and performs a refit adding hits from the segment closest to the extrapolated trajectory, if compatible. Starting from the refit, the algorithm is repeated for each station propagating outward. If no compatible hit is found in two consecutive muon stations, the algorithm stops.

The *Tune-P* algorithm was validated using cosmic ray muons, muons from pp collisions, and Monte Carlo simulations generated using different misalignment scenarios. Both the core and the tails of the momentum, curvature, and invariant mass distributions were studied to ensure that no significant biases in the muon momentum assignment are introduced by the algorithm.

The PF algorithm refines the information from *Tune-P*, exploiting information from the full event, by selecting refits that significantly improve the balance of missing p_{T} and by using a post-processing algorithm designed to preserve events that contain genuine missing energy [17]. The PF momentum assignment was also validated using Monte Carlo simulation and muons from pp collisions.

3.5 Muon isolation

To distinguish between prompt muons and those from weak decays within jets, the isolation of a muon is evaluated relative to its p_{T} by summing up the energy in geometrical cones, $\Delta R = \sqrt{(\Delta\phi)^2 + (\Delta\eta)^2}$, surrounding the muon. One strategy sums reconstructed tracks (track based isolation), while another uses charged hadrons and neutral particles coming from PF (PF isolation).

For the computation of PF isolation [17], the p_{T} of charged hadrons within the ΔR cone originating from the primary vertex are summed together with the energy sum of all neutral particles (hadrons and photons) in the cone. The contribution from pileup to the neutral particles is corrected by computing the sum of charged hadron deposits originating from pileup vertices, scaling it by a factor of 0.5, and subtracting this from the neutral hadron and photon sums to give the corrected energy sum from neutral particles. The factor of 0.5 is estimated from simulations to be approximately the ratio of neutral particle to charged hadron production in inelastic proton-proton collisions. The corrected energy sum from neutral particles is limited to be positive or zero.

For both strategies, tight and loose working points are defined to achieve efficiencies of 95% and 98%, respectively. They are tuned using simulated tight muons from $\mathrm{Z} \to \mu^+\mu^-$ decays with $p_{\mathrm{T}} > 20\,\mathrm{GeV}$. The values for the tight and loose working points for PF isolation within $\Delta R < 0.4$ are 0.15 and 0.25, respectively, while the values for track based isolation within $\Delta R < 0.3$ are 0.05 and 0.10. The efficiency of the working points to reject muons in jets was tested in simulated multi-jet QCD events (events comprised uniquely of jets produced through the strong interaction) and simulated events containing a W boson plus one or more jets (W+jets).

2018 JINST 13 P06015

4 Data and simulated samples

Results shown in this paper come from one of two data sets: approximately 2 fb^{-1} of pp collisions collected in 2015, which will be called "2015 data", and approximately 4 fb^{-1} of pp collisions collected in 2016, which will be called "2016 data". The data set that was used for each result in this paper was chosen depending on the availability of the data and the analyst. In any case, the results represent the CMS muon performance in Run 2 no matter which data set is used, since the peak luminosity delivered by LHC in 2015 and 2016 differed only by about a factor of three, which is small compared to the factor of 40 difference between 2010 and 2016 as described in section 2. The selected data samples consist of events with a pair of reconstructed muons with low p_{T} thresholds. Further event criteria are applied depending on the analyses performed, and are described in detail later.

The performance results most directly applicable to physics analyses are presented in this paper using the 2015 data. These data are compared with simulations from several Monte Carlo event generators for signal and background processes. The Drell-Yan $\text{Z}/\gamma^* \rightarrow \text{l}^+\text{l}^-$ signal sample is generated at next-to-leading order (NLO) with MadGraph5_aMC@NLO 2.3.3 [19]. The background samples of W+jets and of $\text{t}\bar{\text{t}}$ pairs with one or more jets ($\text{t}\bar{\text{t}}$ +jets) are also produced with the same generator. The background from single top quark tW production is generated at NLO with POWHEG v1.0 [20]. The PYTHIA 8.212 [21, 22] package is used for QCD events enriched in muon decays, parton showering, hadronization, and simulation of the underlying event via tune CUETP8M1 [23], using NNPDF2.3 LO [24] as the default set of parton distribution functions. For all processes, the detector response is simulated using a detailed description of the CMS detector based on the GEANT4 package [25] and event reconstruction is performed with the same algorithms as used for the data. The simulated samples include pileup, and the events are weighted so that the pileup distribution matches the 2015 data, having an average pileup of about 11.

5 Spatial resolution

The spatial resolution of a muon subdetector is quantified by the width of the distribution of residuals between the reconstructed and expected hit positions. The expected position is estimated from the segment fit. The resolution is obtained from the residual width by applying standard analytical factors calculated from the "hat matrix" that relates the residuals from a fit to the fitted measurements, and hence the widths of the residual distributions to the intrinsic resolution of the measurements [26]. These factors differ for CSC, in which the reconstructed hit used for the residual is excluded from the segment fit, and for DT where the hit is included. Both CSCs and DTs are designed to make a precise measurement in the direction of bending of a muon track because this directly affects the measurement of the momentum. This is the azimuthal direction, measured in the CSCs by the strips, and in the DTs by the ϕ superlayers.

The spatial resolution of the DTs is determined by computing the value of the residual for each hit used to reconstruct each segment. Typically, eight residual values are computed for each ϕ segment and four for each θ segment. Due to the azimuthal symmetry of the DTs, a single residual distribution is filled with all hits having the same wire orientation from all chambers in the same wheel and station. The width of each residual distribution is converted to position resolution using the standard analytically computed factors described above. Figure 3 shows the spatial resolution

2018 JINST 13 P06015

of DT hits sorted by station, wheel, and wire orientation. The resolution in the ϕ superlayers (i.e., in the bending plane) is better than 250 μm in MB1, MB2 and MB3, and better than 300 μm in MB4. In the θ superlayers, the resolution varies from about 250 to 600 μm except in the outer wheels of MB1.

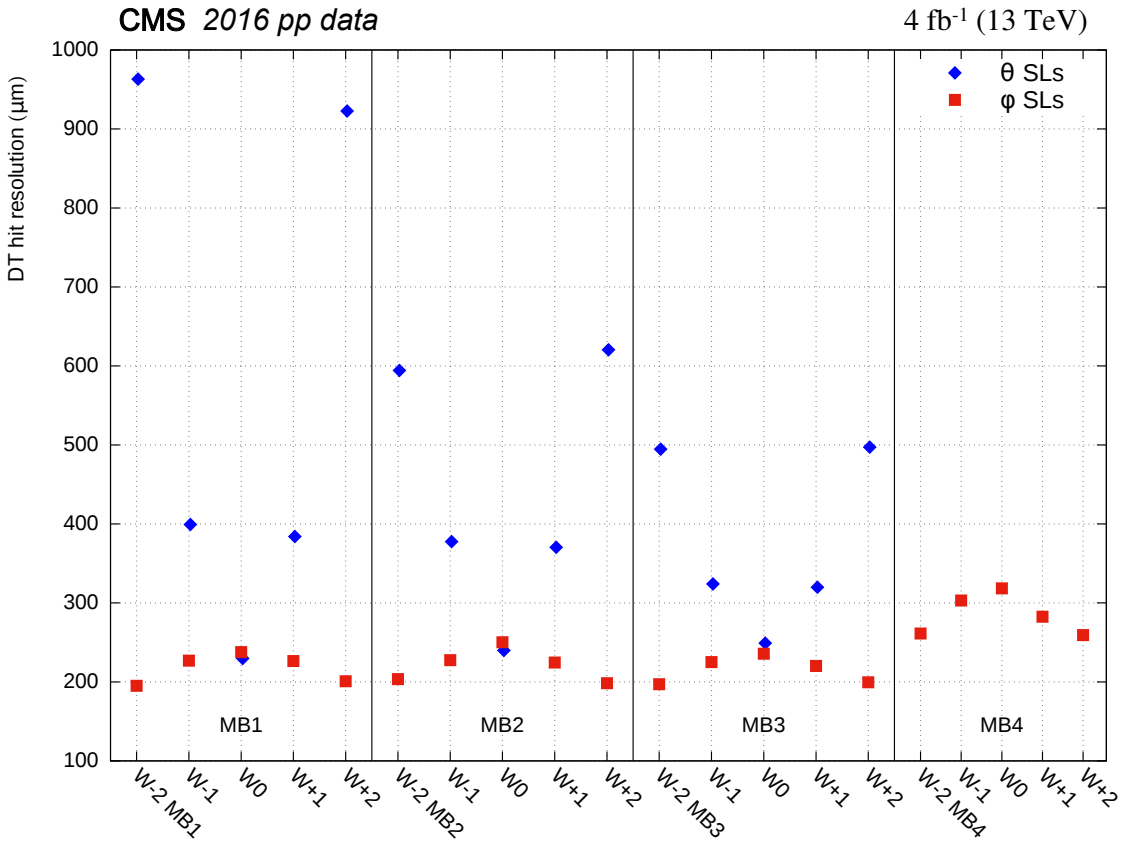

Figure 3. Reconstructed hit resolution for DT ϕ superlayers (squares) and DT θ superlayers (diamonds) measured with the 2016 data, plotted as a function of station and wheel. The uncertainties in these values are smaller than the marker size in the figure.

Within every station, both θ and ϕ superlayers show symmetric behavior with respect to the $z = 0$ plane, as expected from the detector symmetry. In wheel 0, where tracks from the interaction region are mostly perpendicular to all layers, the resolution is the same for θ and ϕ superlayers. From wheel 0 toward the forward region, tracks from the interaction region have increasing values of $|\eta|$; this affects θ and ϕ superlayers in opposite ways. In the θ superlayers the increasing inclination angle degrades the linearity of the distance-drift time relation, thus worsening the resolution. In contrast, in ϕ superlayers the inclination angle increases the track path within the tube (along the wire direction), thus increasing the ionization charge and improving the resolution. The resolution of the ϕ superlayers is worse in MB4 because no θ measurement is available, so no corrections can be applied to account for the muon time of flight and the signal propagation time along the wire. The DT spatial resolution in the 2016 data is improved by about 10% compared to the 2010 results [1] as a result of the improved track reconstruction method in Run 2 that removes spurious early hits, produced by delta rays, from the segment reconstruction (see section 3.1).

2018 JINST 13 P06015

Table 2. CSC transverse spatial resolution per station (6 hits) measured for all chamber types with 2016 data, compared to those measured in 2015 and 2012.

Station/ring	Spatial resolution (μm)		
	Run 1	Run 2	
	2012	2015	2016
ME1/1a	66	48	45
ME1/1b	57	54	52
ME1/2	93	93	90
ME1/3	108	110	105
ME2/1	132	130	125
ME2/2	140	142	134
ME3/1	125	125	120
ME3/2	142	143	135
ME4/1	127	128	123
ME4/2	147	143	134

The spatial resolution of the CSCs is studied using locally reconstructed segments that have exactly one hit per layer. For each segment, the hit in one layer is dropped and the segment is re-fitted with the remaining five hits. The residual between the dropped hit and the new fit is calculated as $R\,\Delta\phi$ in the R-ϕ plane, which is the precision coordinate measured by the strips and the direction of the magnetic bending of the muon. This procedure is repeated for each layer. These residuals are approximately Gaussian and the residual widths are converted to position resolution by using standard analytical factors [26]. The spatial resolution of the CSC strip measurement depends on the relative position at which a muon crosses a strip: it is better for a muon crossing near a strip edge than at the center because then more of the induced charge is shared between that strip and its neighbor, allowing a better estimate of the center of the charge distribution. To benefit from this fact, alternate layers in a CSC are staggered by half a strip width, except in the ME1/1 chambers where the strips are narrower and the effect is small. Resolutions are measured separately for the central half of a strip width (σ_{C}) and the quarter strip-width at each edge (σ_{E}) [1]. The layer measurements are combined to give an overall resolution σ per CSC station by $1/\sigma^2_{\mathrm{station}} = 6/\sigma^2_{\mathrm{layer}}$ (ME1/1 chambers) and $1/\sigma^2_{\mathrm{station}} = 3/\sigma^2_{\mathrm{C}} + 3/\sigma^2_{\mathrm{E}}$ (chambers other than ME1/1). Table 2 summarizes the mean spatial resolution in each CSC station and ring. The design specifications for the spatial resolutions in the CSC system were 75 μm for ME1/1 chambers and 150 μm for the others. These resolutions were chosen so that the contribution of the chamber spatial resolution to the muon momentum resolution is less than or comparable to the contribution of multiple scattering.

The precision of the CSC measurements is dominated by systematic effects, and the statistical uncertainties arising from the fits to the residual distributions are small (<0.2%). The precision is controlled by the size of the induced charge distribution on the strip plane, which is affected by geometry (the width of the strips), gas gain (high voltage, gas mix, gas pressure), and sample selection

2018 JINST 13 P06015

(momenta, angle of incidence). The gas mix and high voltage are stringently maintained constant during CSC operation, and muon samples are selected to be as close as possible for the purposes of these comparisons. The CSCs operate at atmospheric pressure, but a decrease of atmospheric pressure of 1% increases the gas gain by approximately 7%, so the values in the table have all been normalized to 965 mbar, a value typical of the annual average atmospheric pressure at CMS. In this manner we obtain reproducible resolutions typically within 1–2 μm, as can be seen from the values in table 2 for the columns for 2012 and 2015 (other than for ME1/1a). The approximately 25% improvement in resolution in ME1/1a CSCs between 2012 and later is because of the removal of the strip ganging that was used in the first CMS running periods. The improved resolution is not directly related to the spatial nature of the ganging — every 16th strip was ganged into a single channel, rather than combining neighboring strips. Instead, the improvement is because of the reduction of capacitance, and hence noise, with the removal of this ganging. The spatial resolution values for 2016 are systematically better than expected, and this was eventually traced to an incorrectly calibrated gas flowmeter that led to a slightly increased argon fraction in the gas mix in early 2016. Once this was corrected[1] the measured values returned to those seen in earlier running periods.

The spatial resolution of the RPCs is studied by extrapolating segments from the closest CSC or DT to the plane of strips in the chamber under study. The residuals are calculated transverse to the direction of the strips, which is also the direction of the bending of muons in the magnetic field. The residual is defined as the transverse distance between the center of the reconstructed RPC cluster and the point of intersection of the extrapolated segment with the plane of strips. For each station and layer, a residual distribution is filled and fit with a Gaussian. The σ parameter of these fits varies between 0.78–1.27 cm in the barrel and 0.89–1.38 cm in the endcap. These values are compatible with the resolution expected from the widths of the strips and are consistent with the 2010 results [1].

The spatial compatibility between tracker tracks, reconstructed with the inner tracker, and segments, reconstructed in the muon chambers, is of primary importance and is extensively used in the muon ID criteria presented in section 3.2. The residuals between extrapolated tracker tracks and segments are studied using the tag-and-probe technique [2]. Oppositely charged dimuon pairs are selected from a sample collected with a single-muon trigger. The tag is a tight muon with tight PF isolation, which is geometrically matched with the trigger ($\Delta R < 0.1$ between the tracker track and the 4-vector reconstructed by HLT). The probe is a tracker muon, which passes track-based isolation and tracker track quality requirements, that is propagated to each of the DT or CSC chambers it traverses. The segment matching in the definition of a tracker muon is loose enough not to bias this measurement.

The transverse residual, Δx, is computed in the chamber local reference frame for the coordinate measuring the muon position in the bending plane (ϕ). It corresponds to the distance between the position of the propagated tracker track and the segment in the chamber. The RMS of the distribution of Δx is shown in figure 4 for 2015 data and simulated $Z/\gamma^* \rightarrow l^+l^-$ decays. There is reasonable agreement between the data and simulation. The alignment precision of the data (using the techniques described in ref. [27] with the full 2015 data set) and of the simulation (corresponding to what would be obtained with about 1 fb^{-1} of data) is about 100–200 μm, and

[1]Better spatial resolution is not the only consideration in choice of gas mix for CSC operation in CMS. The gas mix is just one of many parameters of the system design that were optimized to provide the required spatial resolution while maintaining stable and robust operation of the detectior and maximum longevity of the chambers in the LHC environment.

2018 JINST 13 P06015

thus is not a dominant effect in these results. Figures 4a and 4b show the RMS as a function of station for DT and CSC chambers, respectively. The RMS increases as the muon station number increases, which is expected because of the larger amount of material traversed by the muons and the resultant multiple scattering. The RMS of the residual evaluated in the first muon station is shown as a function of momentum in figure 4c and figure 4e in the barrel and endcap regions, respectively, while figure 4d shows the overlap region between the two. The RMS decreases with momentum because of the reduction in multiple scattering. The spatial resolution in figure 4 is not directly comparable with the results in ref. [2] because the analysis used on the 2015 data reduced the contamination from muons that do not come from the primary interaction.

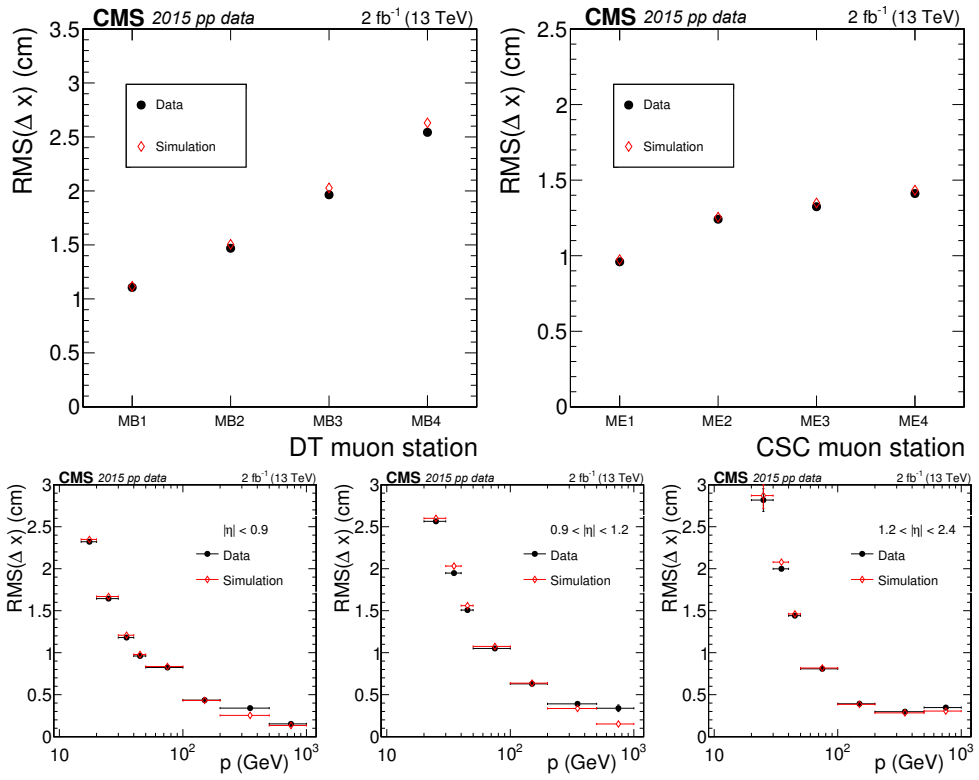

Figure 4. The RMS of transverse residuals between reconstructed segments and propagated tracker tracks, measured in 2015 data. Results are plotted as a function of: (upper left) MB station in the DTs; (upper right) ME station in the CSCs; (lower left) momentum p in station 1 of the barrel region ($|\eta| \leq 0.9$); (lower center) momentum p in station 1 of the overlap region ($0.9 \leq |\eta| \leq 1.2$); (lower right) momentum p in station 1 of the endcap region ($1.2 \leq |\eta| \leq 2.4$). The vertical error bars represent the statistical uncertainties of the RMS, and are smaller than the marker size for most data points.

6 Efficiency

6.1 Hit and segment efficiency

The hit reconstruction efficiency is calculated as the ratio of the number of reconstructed hits divided by the number of expected hits. The measurement provided by the detecting unit under study is excluded from the computation of the expected hit position.

2018 JINST 13 P06015

The hit reconstruction efficiency of the DTs is studied using segments. To ensure high quality segment reconstruction, segments are required to have at least one reconstructed hit in all layers except the layer under study. For the efficiency of a ϕ layer, this implies that the ϕ segment must have at least seven associated hits, while for θ layers, the θ segment must have at least three associated hits. In addition to the high quality of the segment in the view under study, there must be a segment constructed in both ϕ and θ views to ensure the presence of a genuine muon crossing the chamber. For ϕ superlayers, backgrounds are reduced by requiring the segment inclination to be smaller than 45°(by construction, muons from the interaction region are mostly orthogonal to the wire plane). The intersection of this segment with the layer under study determines the position of the expected hit within a specific tube and increments the denominator in the efficiency calculation. The numerator is incremented if a hit is reconstructed in this tube. The distribution of the hit reconstruction efficiency for each DT chamber is shown in figure 5a. The average value of the DT hit reconstruction efficiency is 97.1% including the dead cells reported in table 1. The average efficiency in the 2016 data is consistent with the 2010 average [1] within 1%.

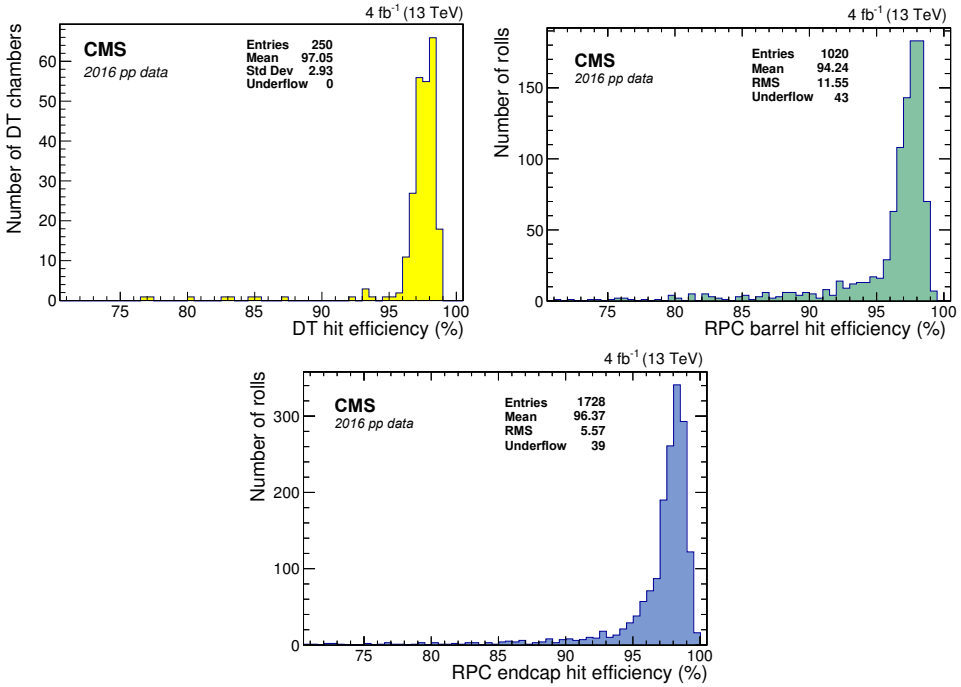

Figure 5. Hit reconstruction efficiency measured with the 2016 data in (upper left) DT, (upper right) RPC barrel, and (lower) RPC endcap chambers.

The hit reconstruction efficiency of the RPCs is studied with a tag-and-probe technique. Muon pairs are selected from an event sample collected with a single-muon trigger. The tag is a tight muon that is geometrically matched with the trigger ($\Delta R < 0.1$ between the tracker track and the 4-vector reconstructed by HLT). The probe is a tracker muon matched to a DT or CSC segment that is extrapolated to RPC chambers. For each RPC roll that the extrapolated probe traverses, the denominator in the efficiency calculation is incremented and a matching hit is sought. The numerator is incremented if the absolute value of the difference between the hit position and the

2018 JINST 13 P06015

extrapolated probe position is smaller than 10 cm, or if the ratio of this distance to its uncertainty (pull), including the extrapolation uncertainty, is less than 4. Figures 5b and c show the efficiency for all RPC barrel and endcap rolls, respectively. The average hit efficiency is 94.2% for the RPC barrel and 96.4% for the RPC endcaps, with negligible accidental contributions from noise. The underflow entries are from rolls with efficiency lower than 70% caused by known hardware problems: chambers with gas leaks in the barrel, and low voltage problems in the endcap. The rolls with zero efficiency (table 1) are included in the underflow and the average efficiency. Results on RPC hit efficiency from 2010 [1] and 2016 are consistent within 1%.

Muons rarely fail to traverse an entire CSC so the CSC readout system [3] requires hits compatible with a charged track crossing a chamber, which suppresses readout of hits from several sources of uninteresting background. In order to read out a cathode front-end board, which services 16 strip channels in each of the six layers of a CSC, the basic pattern of hits expected for a CSC trigger primitive must occur in coincidence with a level-1 trigger from CMS. A trigger primitive requires at least 4 layers in a CSC containing strip hits, with a pattern consistent with those created by muons originating at the pp collision point. This readout suppression complicates the interpretation of straightforward measurements of CSC layer-by-layer hit efficiencies, but since the muon track reconstruction uses segments, and not individual hits, it is the segment efficiency that is most important to system operation. This can be directly measured using the tag-and-probe method. The tag is required to be a tracker muon and the probe is a tracker track that is projected to the muon system. To reduce background and ensure that the probe actually enters the chamber under consideration, compatible hits are also required in a downstream CSC. In the case of station 4, an upstream segment is required. Figure 6 shows a summary map of the measured reconstructed segment efficiency for each CSC. The average CSC segment reconstruction efficiency is 97.4%. A few of the 540 chambers have known inefficiencies, usually caused by one or more faulty electronics boards that cannot be repaired without major intervention requiring the dismantling of the system. There are also occasional temporary failures of electronics boards that last for a few hours or days and can be recovered without major intervention. Both contribute to a reduced segment efficiency in a localized region. The average CSC segment efficiency in the 2016 data is within 1% of that observed in 2010 [1].

6.2 Reconstruction, identification and isolation efficiency

The efficiency for muons is studied with the tag-and-probe method beginning with tracker tracks as probes. The value of the efficiency is computed by factorizing it into several components [2]:

$$\epsilon_\mu = \epsilon_{\text{track}} \times \epsilon_{\text{reco+ID}} \times \epsilon_{\text{iso}} \times \epsilon_{\text{trig}}. \tag{6.1}$$

Each component of ϵ_μ is determined individually. The efficiency of the tracker track reconstruction is ϵ_{track} [14]. The reconstruction+ID efficiency, $\epsilon_{\text{reco+ID}}$, contains both the efficiency of muon reconstruction in the muon system, including the matching of this muon to the tracker track, and the efficiency of the ID criteria. The efficiency of muon isolation, ϵ_{iso}, is studied relative to a probe that has passed the specified muon ID. The efficiency of the trigger, ϵ_{trig}, is described in detail in section 9.2. The application of eq. (6.1) is dependent on the specific needs of each analysis. For example, if an analysis does not require isolation, ϵ_{iso} is removed from the equation and ϵ_{trig} is computed relative to reconstructed muons without an isolation requirement.

2018 JINST 13 P06015

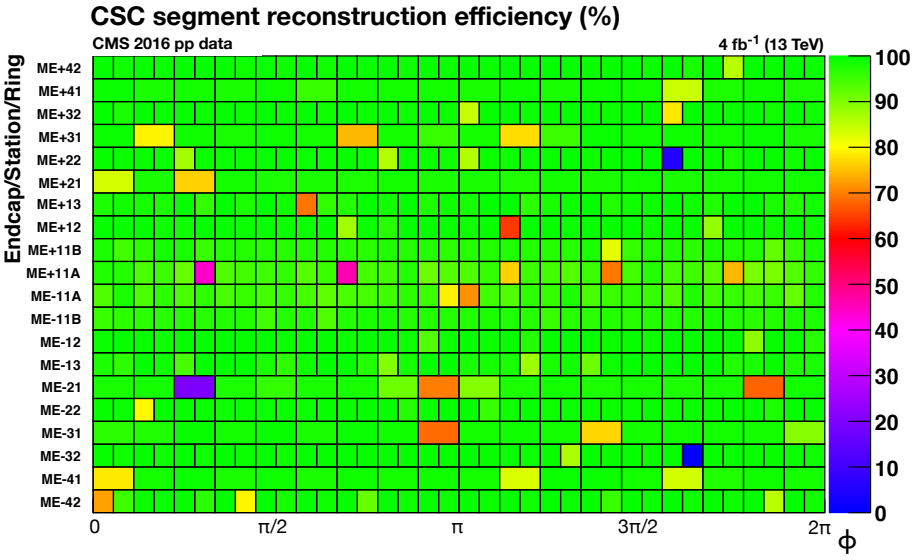

Figure 6. The efficiency (in percent) of each CSC in the CMS endcap muon detector to provide a locally reconstructed track segment as measured from 2016 data.

As described in ref. [2], the combinatorial background of tag-probe pairs not coming from the Z resonance (where the probe is usually a charged hadron misidentified as a muon) is subtracted by performing a simultaneous fit to the invariant mass spectra for passing and failing probes with identical signal shape and appropriate background shapes; the efficiency is then computed from the normalizations of the signal shapes in the two spectra. Given the high multiplicity of tracks in proton-proton collision events, using a tracker track as the probe leads to a high combinatorial background in low-p_{T} bins, which can result in large uncertainties in the background subtraction method. To mitigate this effect, the efficiency measurement is performed using only the tag-and-probe pairs for which a single probe is associated with the tag. The same method is also applied to simulated $\mathrm{Z} \to \mu^{+}\mu^{-}$ events.

The $\epsilon_{\mathrm{reco+ID}}$ for loose muons and for tight muons are shown as a function of η in figure 7, for both data and simulation. The loose ID efficiency exceeds 99% over the entire η range, and the data and simulation agree to within 1%. As a function of p_{T} between 20 GeV and 200 GeV (where the efficiency is measured with reasonably small uncertainty), the loose ID efficiency is constant with fluctuations well within 1%. The tight ID efficiency varies between 95% and 99%, depending on η, and the data and simulation agree to within 1–3%. The dips in efficiency close to $|\eta| = 0.3$ are due to the regions with less instrumentation between the central muon wheel and the two neighboring wheels. In figure 7b, the simulation is systematically higher than the data as a result of small imperfections in the model, which are revealed by the stringent requirements for a muon to satisfy tight ID criteria. In the endcap, differences between the data and simulation arise when the muon is required to be global with a combined fit that has valid hits in the muon system, whereas in the barrel segment matching and global reconstruction contribute to the discrepancy in a similar way. Tracker track quality constraints contribute to a discrepancy of less than 0.5% over the full η range.

A hadron may be misidentified as a prompt muon if the hadron decays in flight, or if hadron shower remnants penetrate through the calorimeters and reach the muon system (punch-through),

2018 JINST 13 P06015

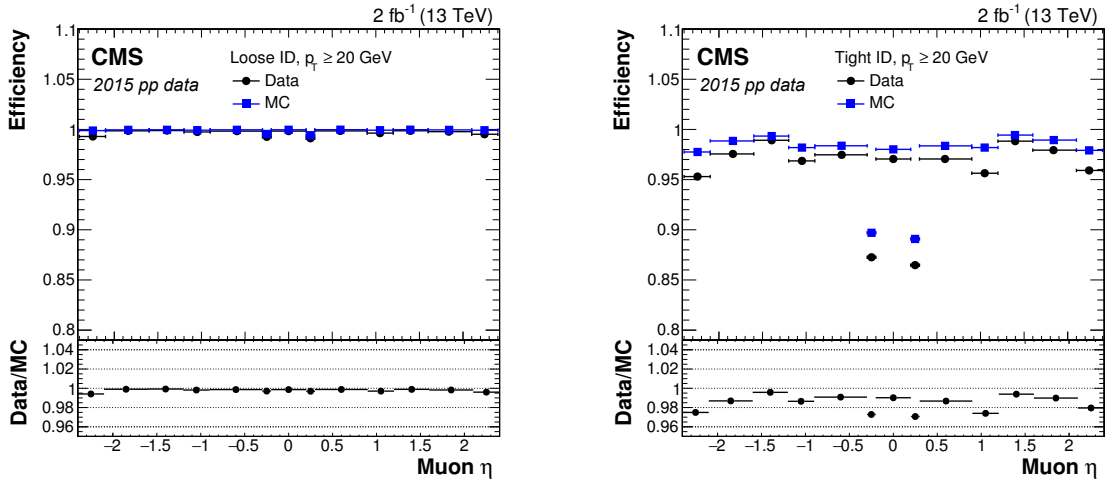

Figure 7. Tag-and-probe efficiency for muon reconstruction and identification in 2015 data (circles), simulation (squares), and the ratio (bottom inset) for loose (left) and tight (right) muons with $p_T > 20$ GeV. The statistical uncertainties are smaller than the symbols used to display the measurements.

or if there is a random matching between a hadron track in the inner tracker and a segment or standalone-muon in the muon system. The probability of hadrons to be misidentified as muons is measured by using data samples of pions and kaons from resonant particle decays collected with jet triggers [2]. The probability of pions to be misidentified as loose muons in both data and simulation is about 0.2% while for tight muons it is about 0.1%. In the same way, 0.5% of kaons are misidentified as loose muons and 0.3% as tight muons in both data and simulation. The uncertainty in these measurements is at the level of 0.05% and is dominated by the limited statistical precision. Within uncertainties, the misidentification probabilities are independent of p_T. These results are in good agreement with Run 1.

The efficiency of muon isolation, ϵ_{iso}, is studied relative to a probe that passes a given muon ID criteria. For example, the tight PF isolation efficiency relative to tight muons is shown in figure 8. In this case the agreement between the data and simulation is always better than 0.5%. Analogous to the misidentification probability study described above, the efficiency to incorrectly label muons within jets as being isolated is measured with simulated QCD events enriched in muon decays. In this sample, the probability of a muon with $p_T > 20$ GeV that fulfills the tight muon ID criteria to also satisfy tight isolation requirements is about 5% in the barrel, and goes up to about 15% in the endcap.

The systematic uncertainty in data/simulation scale factors for the efficiencies described above is estimated by varying the tag-and-probe conditions. The impact of the background contamination is estimated by using different requirements on the tag muon (p_T and isolation) and on the requirement of a single probe being associated with the tag. The dominant uncertainty is caused by the choice of the signal and background models used in the fits. It is estimated by testing alternative fit functions and by varying the range and the binning of the invariant-mass spectrum. The uncertainties are estimated to be at the level of 1% for ID and 0.5% for isolation.

For muons with $p_T > 20$ GeV, table 3 shows the data efficiency and the data/simulation scale factors for the muon ID and isolation working points described in section 3. For all entries,

2018 JINST 13 P06015

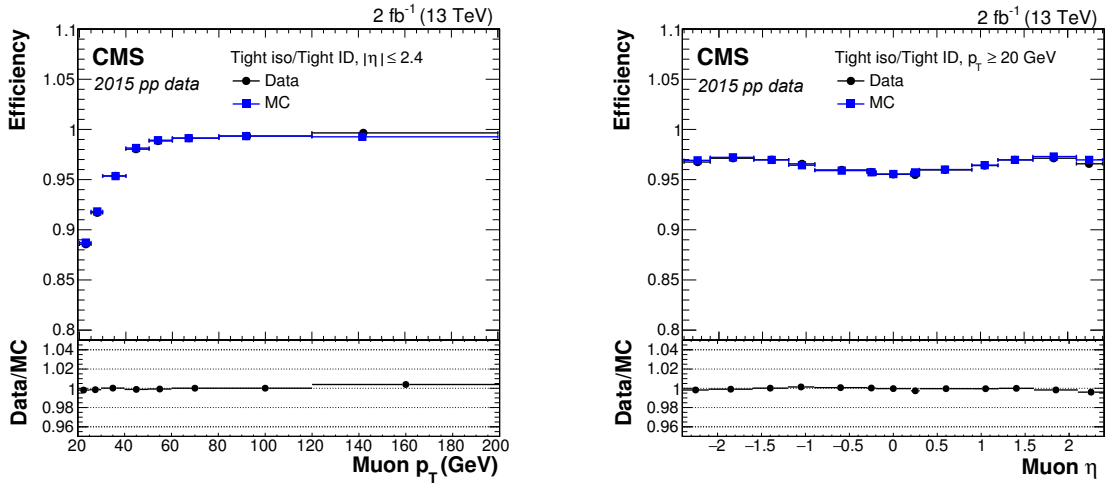

Figure 8. Tag-and-probe efficiency for the tight PF isolation working point on top of the tight ID (left) versus p_T for muons in the acceptance of the muon spectrometer, and (right) versus pseudorapidity for muons with $p_T > 20$ GeV, for 2015 data (circles), simulation (squares), and the ratio (bottom inset). The statistical uncertainties are smaller than the symbols used to display the measurements.

the agreement between data and simulation is better than 1.5%. The efficiencies, systematic uncertainties, and scale factors between data and simulation for 2015 are similar to those found in the 2010 data. The statistical uncertainties, however, have been reduced by a factor of 10 and become negligible in comparison with the systematic uncertainties.

7 Momentum scale and resolution

Many searches for new physics are characterized by signatures involving prompt muons with high p_T. For muons with $p_T > 200$ GeV, combining information from the muon system with information from the inner tracker significantly improves the momentum measurement [28]. On the other hand, for muons with lower p_T the momentum measurement is dominated by the performance of the inner tracker. To assess the performance of the momentum scale and resolution, data from both cosmic rays and collisions have been analyzed.

7.1 Low and intermediate p_T: scale and resolution with collisions

For muons with low and intermediate p_T, two different methods are utilized in Run 2 to correct the muon momentum scale and to estimate the resolution. One method derives the corrections from the mean value of the distribution of $1/p_T^{\mu}$, $\langle 1/p_T^{\mu} \rangle$, for tight muons from Z decays, with further tuning performed using the mean of the dimuon invariant mass spectrum, $\langle M_{\mu\mu} \rangle$ [29]. Another method determines corrections using a Kalman filter on tight muons from J/ψ and Υ(1S) decays [30]. The magnitudes of the momentum scale corrections are about 0.2% and 0.3% in the barrel and endcap, respectively. After the scale is corrected, the resolution is determined either as a function of η (first method) or as a function of η and p_T (second method), including contributions from multiple scattering, position error, and additional smearing to make the simulation match the data. The resolution for muons with momenta up to approximately 100 GeV is 1% in the barrel and 3% in the

2018 JINST 13 P06015

Table 3. Efficiencies for several reconstruction+ID algorithms and isolation criteria (relative to tight ID) for muons with $p_T > 20$ GeV. The corresponding scale factors are for 2015 data relative to simulation. The uncertainties in the scale factors stem from the statistical uncertainties in the fitting procedure. Systematic uncertainties are described in the text.

Type	Label	$\lvert\eta\rvert$ region	Data eff. [%]	Scale factor
Muon ID	Loose	$0.0 < \lvert\eta\rvert < 0.9$	99.75 ± 0.02	0.998 ± 0.001
		$0.9 < \lvert\eta\rvert < 2.4$	99.77 ± 0.02	0.9982 ± 0.0002
	Medium	$0.0 < \lvert\eta\rvert < 0.9$	98.25 ± 0.02	0.9901 ± 0.0002
		$0.9 < \lvert\eta\rvert < 2.4$	98.55 ± 0.02	0.9897 ± 0.0002
	Tight	$0.0 < \lvert\eta\rvert < 0.9$	96.00 ± 0.03	0.9869 ± 0.0004
		$0.9 < \lvert\eta\rvert < 2.4$	97.46 ± 0.04	0.9873 ± 0.0002
	High-p_T	$0.0 < \lvert\eta\rvert < 0.9$	96.24 ± 0.02	0.9882 ± 0.0003
		$0.9 < \lvert\eta\rvert < 2.4$	98.05 ± 0.01	0.9891 ± 0.0002
Isolation (relative to tight ID)	Loose PF	$0.0 < \lvert\eta\rvert < 0.9$	98.60 ± 0.01	1.0007 ± 0.0001
		$0.9 < \lvert\eta\rvert < 2.4$	98.98 ± 0.01	1.0007 ± 0.0001
	Tight PF	$0.0 < \lvert\eta\rvert < 0.9$	95.81 ± 0.02	1.0001 ± 0.0004
		$0.9 < \lvert\eta\rvert < 2.4$	96.88 ± 0.02	0.9995 ± 0.0003

endcap. For both techniques, over all η and p_T values, the uncertainty in the resolution is estimated to be about 5% of its value. Compared to the 2010 results [2], the 2015 resolution has improved, primarily because of the improvements to the tracker alignment [27].

7.2 Momentum resolution with cosmic rays

Cosmic ray muons passing through the CMS detector are used to estimate the momentum resolution at high p_T by comparing the momentum measured in the upper half of the detector with the momentum measured in the lower half [2, 15]. Events are selected with muons that cross the detector close to the interaction point and have at least one hit in the pixel detector, so that each leg of the cosmic ray mimics a muon from a collision. To ensure good reconstruction, the tracker track of each muon leg is required to have at least one pixel hit as well as five strip layers. The relative q/p_T residual, $R(q/p_T)$, is computed as

$$R(q/p_T) = \frac{1}{\sqrt{2}} \frac{(q/p_T)_{\text{upper}} - (q/p_T)_{\text{lower}}}{(q/p_T)_{\text{lower}}}, \tag{7.1}$$

where q is the muon charge, and upper and lower refer to the muon tracks reconstructed in the upper and lower halves of the CMS detector, respectively. The quantity q/p_T, proportional to the muon trajectory curvature, has a symmetric, approximately Gaussian, resolution distribution. The factor of $\sqrt{2}$ accounts for the fact that the q/p_T measurements of the two tracks are independent.

Figure 9 shows the RMS of $R(q/p_T)$ as a function of p_T for cosmic rays recorded in 2015 for fits using only the inner tracker and for fits that include the muon system using the *Tune-P* algorithm.

2018 JINST 13 P06015

The uncertainty in the last bins is dominated by the small number of cosmic rays collected in 2015 (66 events with $p_T > 500$ GeV). The improvement in resolution from exploiting the muon chamber information in the momentum assigment is clearly visible. The simulation of cosmic rays with $p_T > 500$ GeV reproduces this result within statistical uncertainties. Compared with the 2010 results, the resolution is improved by about 25% at high p_T, coming as a result of the modifications to the *Tune-P* algorithm in addition to the improved alignment of both the inner tracker [27] and the muon system [1].

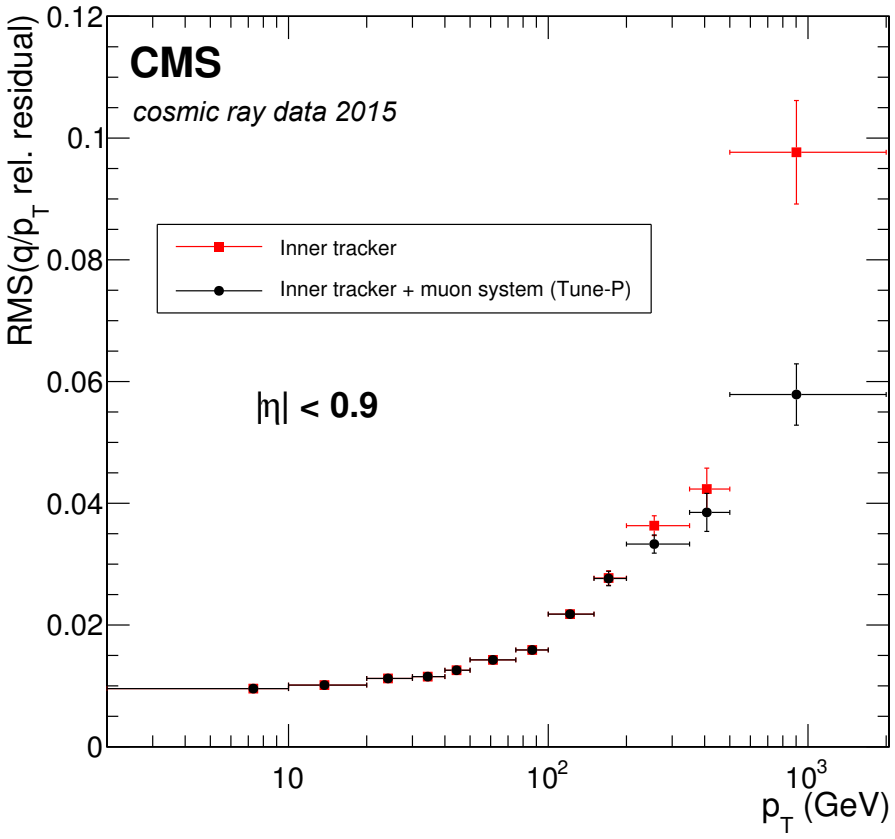

Figure 9. The RMS of $R(q/p_T)$ as a function of p_T for cosmic rays recorded in 2015, using the inner tracker fit only (squares) and including the muon system using the *Tune-P* algorithm (circles). The vertical error bars represent the statistical uncertainties of the RMS.

7.3 High p_T: momentum scale with collisions

Biases in the scale of the momentum measurement at high p_T arising from an inaccurate measurement of the track curvature are probed by looking for distortions in the shape of the q/p_T spectrum. A technique called the "endpoint method" was developed and used extensively in Run 1, using cosmic ray data to quantify the bias at high p_T [1, 2]. However, since cosmic rays predominantly cross the barrel region of the detector, they cannot be used effectively to determine the momentum scale in the endcaps. Therefore, a generalized version of the endpoint method has been developed to be used with collisions.

2018 JINST 13 P06015

Table 4. Measurement of the momentum scale bias in 2015 data, obtained with the generalized endpoint method using muons with $p_T > 200\,\text{GeV}$ from pp collision data. Results are presented in three η bins corresponding to the barrel and endcap regions.

η range	$-2.4 < \eta < -1.2$	$-1.2 < \eta < 1.2$	$1.2 < \eta < 2.4$
$\langle k_b \rangle$ (1/TeV)	-0.01 ± 0.06	-0.01 ± 0.03	0.01 ± 0.05

The generalized endpoint method uses prompt dimuons selected from a sample of events collected with the single-muon trigger (see section 9). Both muons must satisfy the loose tracker relative isolation criteria and at least one of the muons is required to have $p_T > 200\,\text{GeV}$. This sample is primarily composed of muons from Z/γ^* decays, with a minor contribution from dileptonic decays of $t\bar{t}$ pairs and from diboson production.

Each muon from the event that has $p_T > 200\,\text{GeV}$ is used to fill a binned distribution of q/p_T. The q/p_T data spectrum is compared to multiple samples of simulated muons. Each sample, i, is simulated with a curvature bias, k_b^i, injected on top of an unbiased geometry. The bias shifts the unbiased q/p_T spectrum by

$$q/p_T \rightarrow q/p_T + k_b^i. \tag{7.2}$$

The samples are generated with k_b^i in steps of 0.01/ TeV between −1.00/ TeV and +1.00/ TeV. For each sample, the χ^2 is computed between the unweighted data distribution and the weighted simulation distribution. The value of χ^2 is plotted as function of k_b^i and fit with a second-degree polynomial. The value of k_b^i that gives the minimum fit χ^2 is taken as the curvature bias in the data, k_b. The statistical uncertainty in k_b corresponds to half the range over which the χ^2 increases by one.

The momentum scale bias in 2015 data from the generalized endpoint method is shown in table 4. The bias is presented separately for the barrel and endcaps and integrated over ϕ. Within the statistical uncertainties, the measurements are consistent with no bias. In both the barrel and endcaps, the amplitude of the azimuthal dependence of k_b is less than 0.1/ TeV. The limited statistical precision of the data precludes detailed studies of the ϕ dependence and a detailed analysis of the width of k_b. An analysis using the cosmic ray endpoint method in the barrel is consistent with table 4. However, the large uncertainties in the cosmic ray data don't constrain the bias better than the collision data alone. The scale bias in the 2015 data is approximately consistent with the scale bias measured in 2010 with cosmic rays [2], within the large uncertainties in the 2010 results.

8 Timing

The "L1 accept" signal, which is broadcast to all subdetectors, initiates the readout of the event. Trigger synchronization is of great importance because as simultaneous hits in multiple chambers are required for an L1 trigger, out-of-time chambers can reduce the overall trigger efficiency. Moreover, if the L1 muon trigger is generated early or late relative to the collision time, it forces readout of the entire detector at the wrong bunch crossing. In this context, the timing performance of the RPC hits and the DT and CSC trigger primitives is discussed in section 9.1.

For physics analyses, the time assigned to the muon hits once the event has been collected and fully reconstructed is also important. This is called the "offline time." For a muon traveling at the

2018 JINST 13 P06015

speed of light, produced in a proton-proton collision, and with the correct bunch crossing assignment, the offline time of any muon chamber hit should be reported as $t = 0$. The readout windows of the muon subsystems are large enough to detect muons from several bunch crossings. Any deviations from 0 may be caused by backgrounds such as cosmic-ray muons, beam backgrounds, chamber noise, or out-of-time pileup, or it may be an indication of new physics such as a slow moving, heavy charged particle.

As described in section 3, the timing information of DT segments is obtained from a 3-parameter fit of segments, so that position, direction and time of a crossing track are determined simultaneously. Single track segments were selected to have hits in both projections (at least five in the ϕ view) and to have an inclination angle below 45°. The σ parameter of a Gaussian fit to the segment time distribution is 2.0 ns, which represents an estimate of the DT segment time resolution. An improvement of about 0.6 ns is observed with respect to the 2010 performance [1]. This improvement results from the updated segment reconstruction algorithm that now explicitly measures the segment time.

The time of a CSC reconstructed segment is determined by combining the times of the cathode and anode hits used to construct the segment. The overall precision depends mostly on the cathode timing performance. The cathode time is determined from a template fit to the digitized cathode pulse. It is calibrated based on dedicated studies of chamber response and a heuristic correction measured from collision data. Figure 10 shows the distribution of times of CSC segments associated with reconstructed muons. The RMS of the binned segment time distribution is 3.2 ns, in good agreement with the value of about 3 ns measured in 2010 [1].

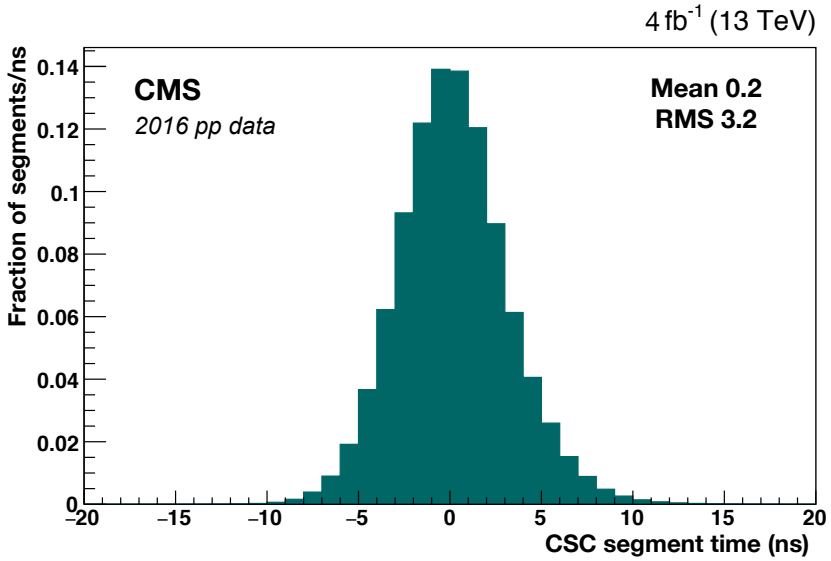

Figure 10. Distribution of times from reconstructed CSC segments measured with the 2016 data.

The timing of a standalone-muon can be determined by combining measurements from multiple stations. In the barrel, measurements from up to four DT stations are combined using an iterative pruning mechanism to discard outlier hits from those associated with the track, thereby rejecting hits from delta rays and showers within an individual chamber. The time-at-vertex distribution for standalone-muons in the barrel is shown in figure 11. This distribution comes from muons that have

2018 JINST 13 P06015

triggered the event readout and shows a primary peak clearly visible at 0 ns. The asymmetric tail at early values comes from delta rays that reach the wire before the hit. The peaks periodically spaced at 25 ns both before and after the primary peak come from muons produced in LHC collisions in bunch crossings that are out of time with regard to the trigger. These secondary peaks come from muons that did not trigger the event readout because of the large suppression factors in the CMS trigger system (described in section 9) but are within the readout range of the event that did cause the trigger. A comparison with an analysis from Run 1 data [31] shows that in 2016 data the width of the primary timing peak in the muon barrel was consistent within 0.5 ns. A similar analysis using the CSC shows comparable muon time resolution.

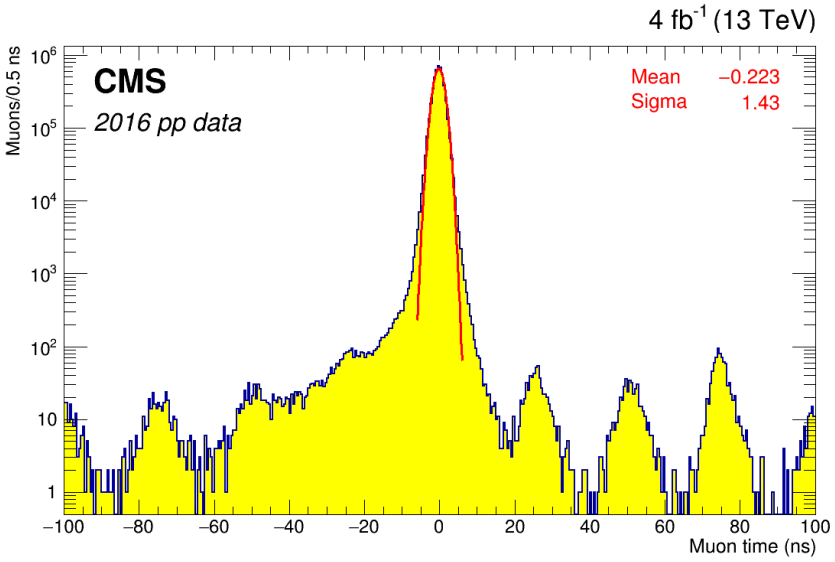

Figure 11. Time-at-vertex distribution for standalone-muons in the barrel, using the times measured by DT chambers in 2016 data.

9 Trigger

For the muon component of the CMS trigger [6], CSC and DT chambers provide "trigger primitives" constructed from hit patterns consistent with muons that originate from the collision region, and RPC chambers provide hit information. The custom-made electronics in the L1 trigger system utilize the chamber information to reconstruct muon trigger candidates with a coarse measurement of p_{T}. An upgrade of the L1 trigger system was implemented between 2015 and 2016 [10]. The results presented here do not depend on the upgraded L1 components.

Events selected by the L1 trigger are passed to the HLT, which uses information from the full CMS detector to reconstruct muons. The HLT algorithms are simplified versions of those described in section 3 in order to reduce computing time and resources, and were updated prior to the 2015 run to improve the performance at higher pileup. The HLT employs two different processing schemes to reconstruct muons. The first scheme uses the L1 candidate as a seed to reconstruct muons at level-2 (L2) using information only from the muon system, and then reconstructs level-3 (L3) muons by combining the L2 muons with information from the inner tracker. This combination is made

2018 JINST 13 P06015

using three algorithms applied sequentially from fastest to slowest, and subsequent algorithms are attempted only if the previous one failed to reconstruct a muon in order to minimize computation time. The first algorithm propagates the L2 trajectory inward to the inner tracker to reconstruct the L3 muon. The second algorithm is similar to the first, except that it combines the L2 muon with hits in the outer layer of the inner tracker to improve its trajectory before propagating it inward. The third algorithm is different from the first two in that it builds tracker tracks with an inside out approach within a region based on the position of the L2 muon. Prior to Run 2, the L3 algorithms were improved to select hits based on χ^2 of the track fit rather than matching in ΔR, and track quality constraints are imposed in the first two algorithms.

The second HLT processing scheme, called "HLT tracker muon reconstruction", was developed prior to Run 2. This scheme employs an algorithm similar to the tracker muon algorithm described in section 3, but is optimized for processing speed. The primary differences are that the HLT version limits the reconstruction of tracker tracks to a region within $\Delta\phi < 0.2$ and $\Delta\eta < 0.35$ of the L1 candidate, and requires $p_T > 10$ GeV for the tracker track seeds.

After reconstruction, muon isolation is evaluated in the HLT by considering the additional tracker tracks and calorimeter energy deposits in a cone with radius $\Delta R = 0.3$ around the muon. Each of the contributions is required to be below a fraction of the muon p_T: scalar sum E_T of PF electromagnetic clusters [17], scalar sum E_T of PF hadronic clusters, and scalar sum p_T of tracker tracks. To exclude contributions that come from the muon itself, a minimum value of ΔR is required to include the tracks or energy deposits in the sum. To account for the effects from pileup, PF cluster sums are corrected using the average energy density [32] in the event, ρ (if the correction exceeds the PF cluster sum, that component of the isolation is set to zero). To determine the correction, the value of ρ is scaled by its "effective area" which estimates how much is expected in the isolation cone. Effective areas are determined independently for electromagnetic sums and for hadronic sums as well as separately in the barrel and in the endcaps. The average values of the distributions of PF cluster sums are fit with a first order polynomial as a function of the number of reconstructed primary vertices. The same is done for ρ. The effective area is the ratio of the fitted slope for the PF cluster sum divided by the fitted slope for ρ.

After minimal ΔR cones and effective areas are defined, a working point is determined to simultaneously remove background effectively and to keep signal efficiency high by tuning the thresholds below which the muon is considered to be isolated. For example, for online isolation in the barrel in 2015, the ρ-corrected scalar sum E_T of PF electromagnetic clusters within $0.05 < \Delta R < 0.3$ were required to be below 11% of the muon p_T, the ρ-corrected scalar sum E_T of PF hadronic clusters within $0.1 < \Delta R < 0.3$ were required to be below 21% of the muon p_T, and the scalar sum p_T of tracker tracks within $0.01 < \Delta R < 0.3$ were required to be below 9% of the muon p_T.

The results of the HLT reconstruction and isolation algorithms are used to form various trigger conditions. The general-purpose muon trigger conditions used for the 2015 data include:

1. an isolated single-muon with a p_T threshold of 20 GeV, which is based on a trigger efficiency curve giving approximately 50% efficiency at 20 GeV [6], reconstructed with either L3 or HLT tracker muon algorithms,

2. a nonisolated single-muon with a p_T threshold of 45 GeV for $|\eta| < 2.1$ or 50 GeV for $|\eta| < 2.4$, reconstructed with L3, and

2018 JINST 13 P06015

3. two isolated muons (double-muons) that originate within a distance of $\Delta z < 0.2\,\text{cm}$ of each other along the beamline, with asymmetric p_{T} thresholds of 18 GeV and 7 GeV applied to the two muons.

For the double-muon triggers, the L3 algorithm is first used to reconstruct one muon. In order to save computing time, this L3 muon must pass p_{T} and quality constraints before reconstruction of a second muon is attempted. The second muon can be reconstructed with either the L3 or the HLT tracker muon algorithm to maximize efficiency. Tracker track isolation criteria are then applied to both tracks.

9.1 Trigger primitives

The absolute efficiency for creating a CSC trigger primitive is studied using the tag-and-probe method in the same way as for CSC segments (section 6). Once again the probe is a tracker track extrapolated into the muon system. The tag is required to have triggered the event to avoid bias from events triggered by the probe alone. A CSC trigger primitive is expected in each chamber traversed by the probe. To reduce background and to ensure that the probe actually entered the chamber under consideration, a compatible segment is required in a downstream chamber. For the outermost station 4 an upstream chamber is required instead. A trigger primitive is required to be within 5 cm of the extrapolated track (corresponding to about 4–5 times the resolution, as demonstrated in figure 4b) with no other track closer to it. The CSC trigger primitive efficiency is shown in figure 12. The features in figure 12 are highly correlated with the features in figure 6 because in both cases the primary causes of significant inefficiencies were hardware failures. The average CSC trigger primitive efficiency in 2016 data is 97%, similar to that in 2010 [1].

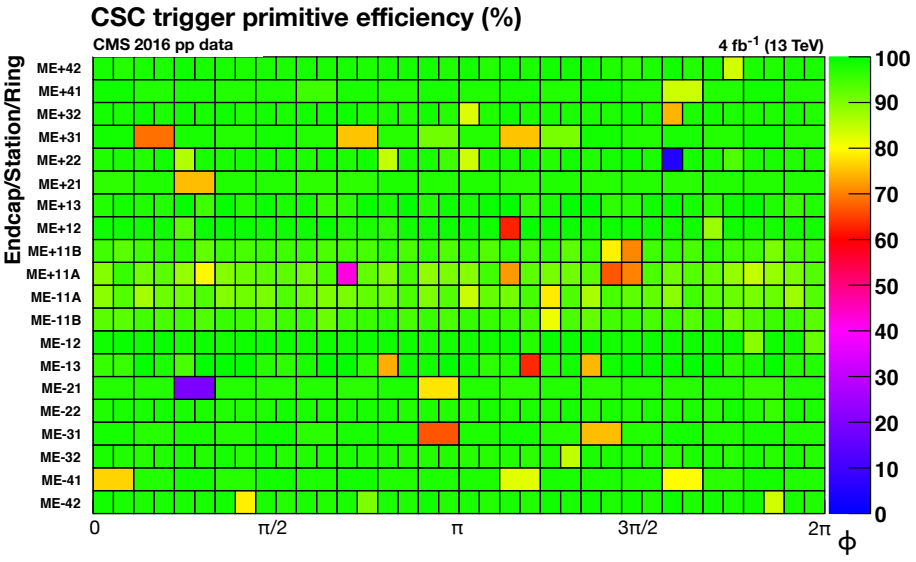

Figure 12. The efficiency (in percent) of each CSC to provide a trigger primitive, measured with the 2016 data.

The efficiency for the DT local trigger electronics to reconstruct a trigger primitive pattern is called the DTLT efficiency, and it can be studied using segments associated with global muons. In

order to ensure that the chamber under study was not necessarily used to trigger the event, at least two other stations are required to deliver trigger primitives. The denominator is incremented if the segment is reconstructed in both θ and ϕ views, except for MB4, which has only ϕ superlayers. In addition, there must be at least four associated hits in the ϕ layers, the minimum number of hits required to build a ϕ trigger primitive. The numerator is incremented if a trigger primitive is delivered at the correct bunch crossing. The DTLT efficiency is shown for each DT chamber in figure 13. The lower DTLT efficiency observed in two of the chambers was due to problems with the trigger electronics which were later repaired. The DTLT efficiency is about 1% lower in MB4 because there are no θ superlayers to enhance the quality of the segment. The DTLT efficiency in the 2016 data is comparable to the one observed in the 2010 data.

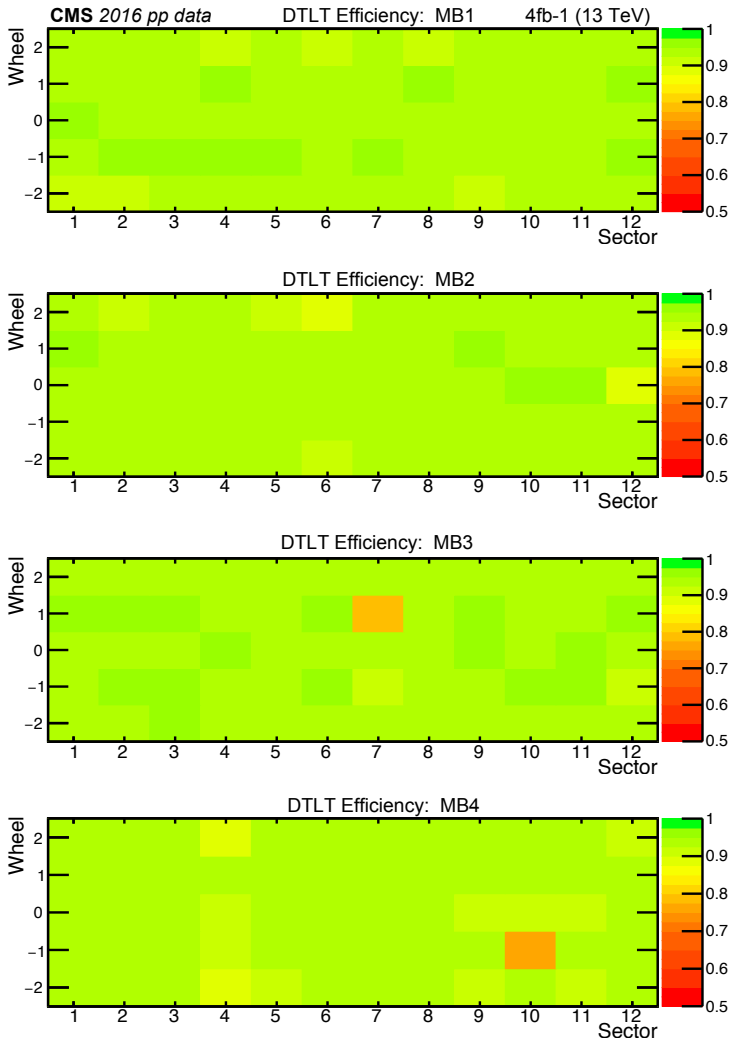

Figure 13. Efficiency map for the DT local trigger (ϕ view) for each chamber, measured with the 2016 data. Each map represents one station. The z-axis color indicates the efficiency, the wheel number is on the vertical axis, and the ϕ sector number is on the horizontal axis.

For RPCs, the trigger primitive efficiency is equivalent to the hit efficiency by construction. The trigger primitive efficiency is shown in figure 5.

2018 JINST 13 P06015

The time coincidence of trigger primitives among the many muon stations must have a time dispersion much less than 25 ns, the time separation of LHC bunch crossings, to ensure an unambiguous identification of the correct bunch crossing with the muon trigger. For example, the RPC chambers have been measured to have an intrinsic time resolution of around 2 ns [33] and an overall time resolution of better than 3 ns [1] after including the time propagation along the strip, the channel-by-channel cable length differences, and the electronics delays. Figure 14 shows the bunch crossing distribution of RPC hits associated with global muons in the barrel. Each bin corresponds to the 25 ns bunch separation in LHC, and bin 0 is the time of the L1 trigger. In figure 14, 0.5% of RPC hits are outside bin 0, whereas for both DT and CSC trigger primitives, 2% are outside bin 0. The hits that are not in bin 0 are caused by a combination of muons from adjacent bunch crossings or from cosmic rays and by the finite resolution in the calibration of the electronics. The timing of each individual system is monitored during data collection and fine adjustments are made if necessary. In this way, the L1 trigger, which relies on a combination of all three systems, produces less than 0.2% trigger candidates associated with incorrect bunch crossings [6].

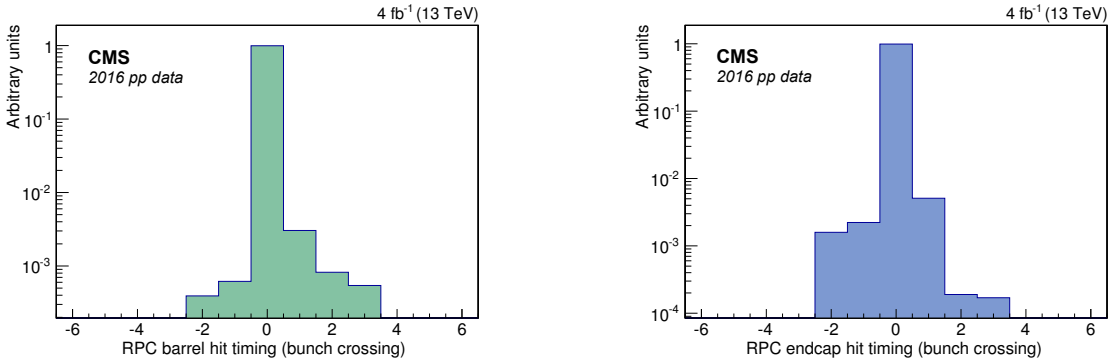

Figure 14. The bunch crossing distribution from reconstructed RPC hits in the barrel (left) and in one endcap (right), using the 2016 data.

9.2 Trigger efficiencies and rates

As described in section 6.2, the efficiency of the trigger is measured with the tag-and-probe technique. In order not to bias the measurement of the trigger efficiency, the tag is geometrically matched to the HLT trigger that selected the event. In addition, it is also required to satisfy tight ID and PF isolation criteria in order to reduce backgrounds. The requirements on the probe are then tuned according to the reconstruction and isolation criteria used in the analysis. As an example, an analysis of muons with tight ID and PF isolation requirements might use the isolated single-muon trigger to select events. In this case, the probe muon is required to satisfy tight ID and PF isolation requirements as per the analysis. Using this technique, the efficiency of the isolated single-muon trigger with HLT p_{T} threshold 20 GeV is shown in figure 15. The efficiency as a function of reconstructed muon p_{T} (figure 15a) rises sharply at the threshold. Above 22 GeV, the inefficiency of a few percent is primarily caused by the L1 trigger and the relative isolation criteria (see table 5). Variations in efficiency as a function of η (figure 15b) are caused by geometrical features of the detector that affect the L1 trigger efficiency. The isolation requirement is responsible for the mild efficiency drop as a

2018 JINST 13 P06015

function of the number of offline reconstructed vertices (figure 15c). The systematic uncertainty is estimated to be 0.5% based on methods similar to those described in section 6. The simulation is in reasonable agreement with the data over the full momentum range and angular acceptance.

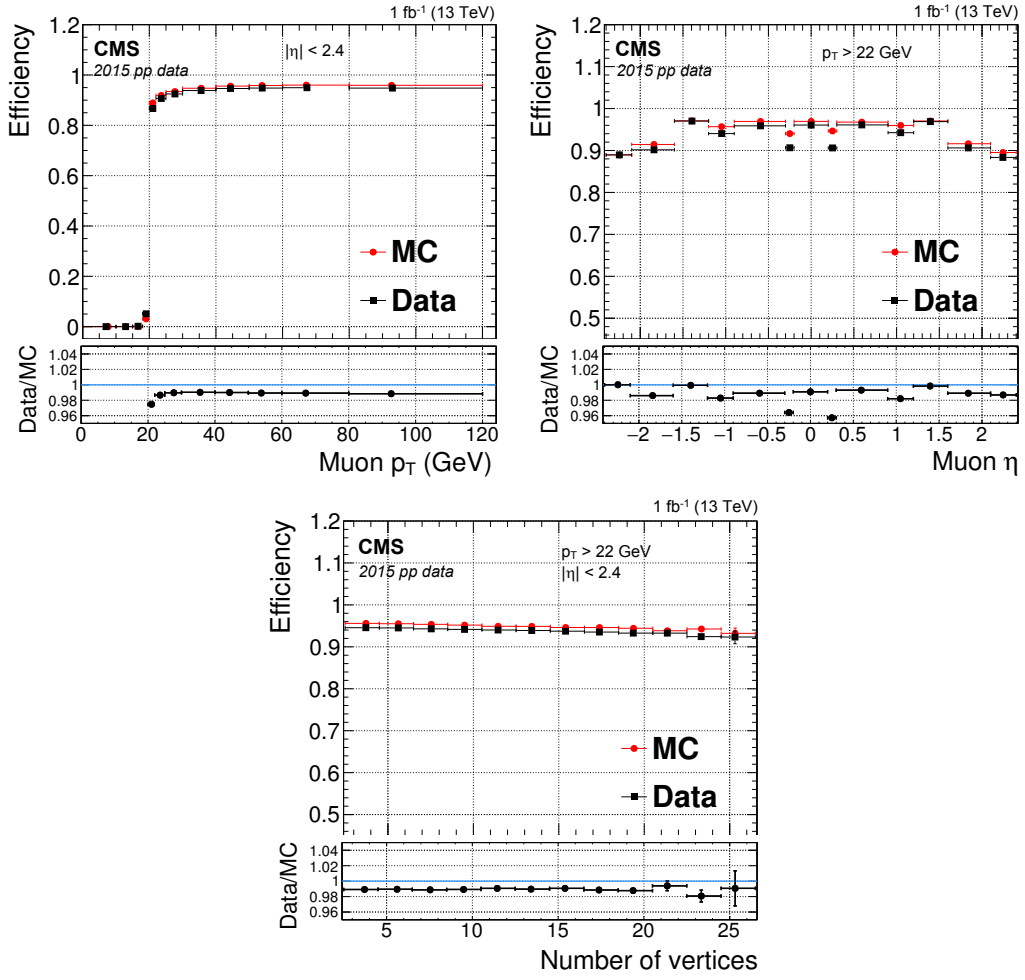

Figure 15. Isolated single-muon trigger efficiency measured with 2015 data (squares), simulation (circles), and the ratio (bottom inset). Results are plotted as a function of offline reconstructed muon p_T (upper left), η (upper right), and number of primary vertices (lower). The statistical uncertainties in these values are smaller than the marker size in the figure.

A breakdown of the contributions to the isolated single-muon trigger efficiency from L1, HLT track reconstruction, and online isolation is presented in table 5, together with the scale factors between data and simulation. Numbers are separated into barrel and endcap regions, and are integrated over offline reconstructed $p_T > 22$ GeV for each row, the momentum range commonly used for CMS physics analyses with isolated single-muon triggers. The first two rows show the efficiency of L1 candidates (p_T threshold 16 GeV) computed with respect to tight muons passing PF isolation criteria. The second two rows show the efficiency of HLT reconstruction (p_T threshold 20 GeV) computed with respect to offline muons geometrically matched to L1 candidates, which are used as the seeds for HLT tracking. The use of two complementary reconstruction algorithms

2018 JINST 13 P06015

Table 5. Contributions to the isolated single-muon trigger efficiency in 2015 data, integrated over $p_T >$ 22 GeV. The first two rows show the level-1 efficiency (p_T threshold 16 GeV) with respect to offline muons. The second two rows show the HLT efficiency (p_T threshold 20 GeV) with respect to offline muons geometrically matched to L1 candidates. The last two rows show the online isolation efficiency with respect to offline muons firing HLT. The uncertainties in these values are statistical.

Step	$\|\eta\|$ region	Data eff. [%]	Scale factor
L1 w.r.t. offline	$0.0 < \|\eta\| < 0.9$	96.86 ± 0.02	0.9914 ± 0.0005
	$0.9 < \|\eta\| < 2.4$	94.38 ± 0.02	0.9947 ± 0.0005
HLT w.r.t. L1	$0.0 < \|\eta\| < 0.9$	99.67 ± 0.02	0.9967 ± 0.0005
	$0.9 < \|\eta\| < 2.4$	99.46 ± 0.02	0.9957 ± 0.0005
Online isolation w.r.t. HLT	$0.0 < \|\eta\| < 0.9$	97.95 ± 0.02	0.9906 ± 0.0005
	$0.9 < \|\eta\| < 2.4$	98.28 ± 0.02	0.9931 ± 0.0005

results in an efficiency exceeding 99% for the HLT reconstruction of isolated single-muon triggers for prompt muons passing L1 trigger requirements. The last two rows show the effect of isolation on top of the HLT reconstruction.

The efficiency for isolated single-muon triggers is improved with respect to Run 1 [2, 6] as a result of a combination of the changes in HLT algorithms, the addition of RPC and CSC chambers in station 4, and the removal of the ganging of strips in ME1/1a. In the endcaps, the improvement in trigger efficiency (L1+HLT+isolation) relative to the end of Run 1 [6] is about 10% for $|\eta| > 1.2$ but reaches 20% for $|\eta| \approx 2.4$.

A comparison of trigger rates at the same instantaneous luminosity and threshold ($p_T >$ 24 GeV), and integrated over $|\eta| < 2.4$, shows an increase of about 75% from Run 1 to Run 2. This increase is approximately consistent with the increase of the inclusive production cross sections for W and Z bosons due to the change from $\sqrt{s} = 8$ TeV [34] to $\sqrt{s} = 13$ TeV [35] with an additional contribution from the increase in efficiency described above.

The combination of the updated HLT algorithms and the overall increase of HLT output rate, together with a different allocation of the bandwidth, made it possible to reduce the p_T thresholds on isolated single-muon triggers from 24 GeV in 2012 to 20 GeV in 2015. The nonisolated triggers operated in 2015 with p_T thresholds of 45 GeV ($|\eta| < 2.1$) and 50 GeV ($|\eta| < 2.4$). For inclusive double-muon triggers, the use of track-based isolation requirements in Run 2 resulted in a reduction of the rates of these triggers with respect to Run 1 despite the increase in collision energy. In 2015, the thresholds for the two muons in double-muon triggers were 18 GeV and 7 GeV, the same values as in 2012.

Figure 16 shows the invariant mass distribution of oppositely charged muon pairs selected by the inclusive trigger on isolated double-muons. The x-axis is logarithmic so the entries are scaled to the width of each bin. Data are also included from specific double-muon triggers tuned to select resonances at low invariant mass. The figure clearly demonstrates the ability of CMS to identify muons, trigger on them, and reconstruct the muon kinematics to unambiguously identify particles that decay into muons over a broad energy range.

2018 JINST 13 P06015

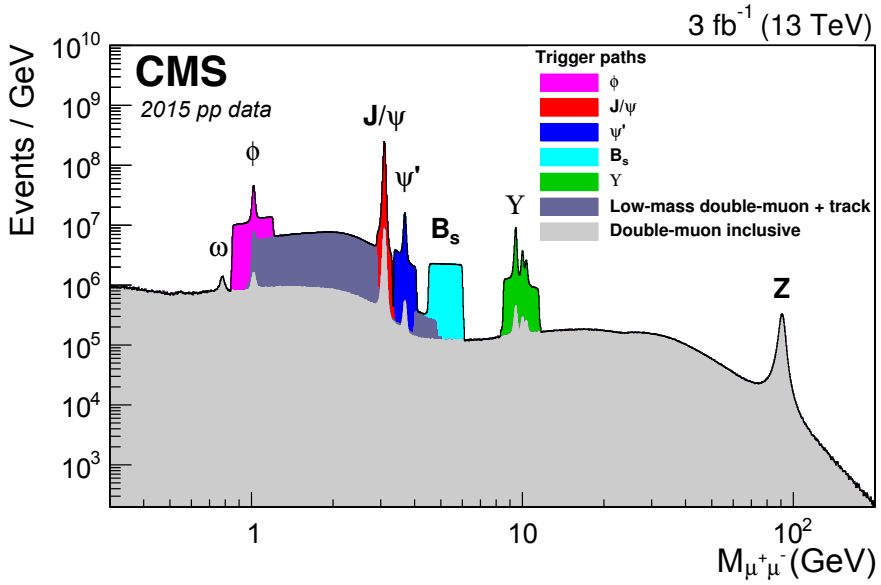

Figure 16. The dimuon invariant mass distribution reconstructed by the CMS HLT. Data were collected in 2015 with the inclusive double-muon trigger algorithm (gray), as well as triggers dedicated to selecting resonances at low masses.

10 Summary

The performance of the CMS muon detector and reconstruction software has been studied using data from proton-proton collisions at center-of-mass energy $\sqrt{s} = 13\,\text{TeV}$, collected in 2015 and 2016 during LHC Run 2. These results are compared to the previously published results collected in 2010 at $\sqrt{s} = 7\,\text{TeV}$ with instantaneous luminosities about a factor of 40 lower. Important modifications to many components of the muon system were made before Run 2 in anticipation of the higher collision energy and the increased luminosity. These included modifications to drift tubes, cathode strip chambers, and resistive plate chambers, as well as improved algorithms for the high-level trigger and offline reconstruction. Although not comprehensive, a set of representative figures of merit for the system performance include:

- reconstructed hit spatial resolution $\approx 50 - 300\,\mu\text{m}$;
- reconstructed hit efficiency $\approx 94 - 99\%$;
- segment timing resolution $< 3\,\text{ns}$;
- segment efficiency $\approx 97\%$;
- trigger bunch crossing identification $> 99\%$;
- trigger efficiency $> 90\%$;
- muon timing resolution $\approx 1.4\,\text{ns}$;
- muon reconstruction and identification efficiency $> 96\%$;
- muon isolation efficiency $> 95\%$.

2018 JINST 13 P06015

As a result of the improvements to the detector and the reconstruction algorithms, and despite the higher luminosity and pileup in Run 2, the muon performance is better than, or at least as good as, it was in 2010. Detector performance remains within the design specifications and the muon reconstruction results are well reproduced by Monte Carlo simulation.

Acknowledgments

We congratulate our colleagues in the CERN accelerator departments for the excellent performance of the LHC and thank the technical and administrative staffs at CERN and at other CMS institutes for their contributions to the success of the CMS effort. In addition, we gratefully acknowledge the computing centers and personnel of the Worldwide LHC Computing Grid for delivering so effectively the computing infrastructure essential to our analyses. Finally, we acknowledge the enduring support for the construction and operation of the LHC and the CMS detector provided by the following funding agencies: the Austrian Federal Ministry of Science, Research and Economy and the Austrian Science Fund; the Belgian Fonds de la Recherche Scientifique, and Fonds voor Wetenschappelijk Onderzoek; the Brazilian Funding Agencies (CNPq, CAPES, FAPERJ, and FAPESP); the Bulgarian Ministry of Education and Science; CERN; the Chinese Academy of Sciences, Ministry of Science and Technology, and National Natural Science Foundation of China; the Colombian Funding Agency (COLCIENCIAS); the Croatian Ministry of Science, Education and Sport, and the Croatian Science Foundation; the Research Promotion Foundation, Cyprus; the Secretariat for Higher Education, Science, Technology and Innovation, Ecuador; the Ministry of Education and Research, Estonian Research Council via IUT23-4 and IUT23-6 and European Regional Development Fund, Estonia; the Academy of Finland, Finnish Ministry of Education and Culture, and Helsinki Institute of Physics; the Institut National de Physique Nucléaire et de Physique des Particules / CNRS, and Commissariat à l'Énergie Atomique et aux Énergies Alternatives / CEA, France; the Bundesministerium für Bildung und Forschung, Deutsche Forschungsgemeinschaft, and Helmholtz-Gemeinschaft Deutscher Forschungszentren, Germany; the General Secretariat for Research and Technology, Greece; the National Research, Development and Innovation Fund, Hungary; the Department of Atomic Energy and the Department of Science and Technology, India; the Institute for Studies in Theoretical Physics and Mathematics, Iran; the Science Foundation, Ireland; the Istituto Nazionale di Fisica Nucleare, Italy; the Ministry of Science, ICT and Future Planning, and National Research Foundation (NRF), Republic of Korea; the Lithuanian Academy of Sciences; the Ministry of Education, and University of Malaya (Malaysia); the Mexican Funding Agencies (BUAP, CINVESTAV, CONACYT, LNS, SEP, and UASLP-FAI); the Ministry of Business, Innovation and Employment, New Zealand; the Pakistan Atomic Energy Commission; the Ministry of Science and Higher Education and the National Science Centre, Poland; the Fundação para a Ciência e a Tecnologia, Portugal; JINR, Dubna; the Ministry of Education and Science of the Russian Federation, the Federal Agency of Atomic Energy of the Russian Federation, Russian Academy of Sciences and the Russian Foundation for Basic Research; the Ministry of Education, Science and Technological Development of Serbia; the Secretaría de Estado de Investigación, Desarrollo e Innovación, Programa Consolider-Ingenio 2010, Plan Estatal de Investigación Científica y Técnica y de Innovación 2013-2016, Plan de Ciencia, Tecnología e Innovación 2013-2017 del Principado de Asturias and Fondo Europeo de Desarrollo Regional, Spain; the Swiss Funding Agencies (ETH

2018 JINST 13 P06015

Board, ETH Zurich, PSI, SNF, UniZH, Canton Zurich, and SER); the Ministry of Science and Technology, Taipei; the Thailand Center of Excellence in Physics, the Institute for the Promotion of Teaching Science and Technology of Thailand, Special Task Force for Activating Research and the National Science and Technology Development Agency of Thailand; the Scientific and Technical Research Council of Turkey, and Turkish Atomic Energy Authority; the National Academy of Sciences of Ukraine, and State Fund for Fundamental Researches, Ukraine; the Science and Technology Facilities Council, U.K.; the US Department of Energy, and the US National Science Foundation.

Individuals have received support from the Marie-Curie program and the European Research Council and Horizon 2020 Grant, contract No. 675440 (European Union); the Leventis Foundation; the A. P. Sloan Foundation; the Alexander von Humboldt Foundation; the Belgian Federal Science Policy Office; the Fonds pour la Formation à la Recherche dans l'Industrie et dans l'Agriculture (FRIA-Belgium); the Agentschap voor Innovatie door Wetenschap en Technologie (IWT-Belgium); the F.R.S.-FNRS and FWO (Belgium) under the "Excellence of Science — EOS" — be.h project n. 30820817; the Ministry of Education, Youth and Sports (MEYS) of the Czech Republic; the Lendület ("Momentum") Programme and the János Bolyai Research Scholarship of the Hungarian Academy of Sciences, the New National Excellence Program ÚNKP, the NKFIA research grants 123842, 123959, 124845, 124850 and 125105 (Hungary); the Council of Scientific and Industrial Research, India; the HOMING PLUS program of the Foundation for Polish Science, cofinanced from European Union, Regional Development Fund, the Mobility Plus program of the Ministry of Science and Higher Education, the National Science Center (Poland), contracts Harmonia 2014/14/M/ST2/00428, Opus 2014/13/B/ST2/02543, 2014/15/B/ST2/03998, and 2015/19/B/ST2/02861, Sonata-bis 2012/07/E/ST2/01406; the National Priorities Research Program by Qatar National Research Fund; the Programa de Excelencia María de Maeztu and the Programa Severo Ochoa del Principado de Asturias; the Thalis and Aristeia programs cofinanced by EU-ESF and the Greek NSRF; the Rachadapisek Sompot Fund for Postdoctoral Fellowship, Chulalongkorn University and the Chulalongkorn Academic into Its 2nd Century Project Advancement Project (Thailand); the Welch Foundation, contract C-1845; and the Weston Havens Foundation (U.S.A.).

References

[1] CMS collaboration, *The performance of the CMS muon detector in proton-proton collisions at* $\sqrt{s} = 7$ *TeV at the LHC*, 2013 *JINST* **8** P11002 [arXiv:1306.6905].

[2] CMS collaboration, *Performance of CMS muon reconstruction in pp collision events at* $\sqrt{s} = 7$ *TeV*, 2012 *JINST* **7** P10002 [arXiv:1206.4071].

[3] CMS collaboration, *The CMS muon project: technical design report*, CERN-LHCC-97-032, CERN, Geneva, Switzerland, (1997).

[4] CMS collaboration, *The CMS experiment at the CERN LHC*, 2008 *JINST* **3** S08004.

[5] CMS collaboration, *CMS TriDAS project — technical design report, volume* 1*: the trigger systems*, CERN-LHCC-2000-038, CERN, Geneva, Switzerland, (2000) [CMS-TDR-6-1].

[6] CMS collaboration, *The CMS trigger system*, 2017 *JINST* **12** P01020 [arXiv:1609.02366].

[7] R. Alemany-Fernandez et al., *Operation and configuration of the LHC in run* 1, CERN-ACC-NOTE-2013-0041, CERN, Geneva, Switzerland, (2013).

2018 JINST 13 P06015

[8] G. Papotti et al., *Operation of the LHC with protons at high luminosity and high energy*, in *Proc. of International Particle Accelerator Conference*, (IPAC 2016), Busan, Korea, May 2016

[9] J. Wenninger, *Approaching the nominal performance at the LHC*, in *Proc. of International Particle Accelerator Conference*, (IPAC 2017), Copenhagen, Denmark, May 2017.

[10] CMS collaboration, *CMS technical design report for the level-1 trigger upgrade*, CERN-LHCC-2013-011, CERN, Geneva, Switzerland, (2013) [CMS-TDR-12].

[11] CMS collaboration, *The CMS barrel muon trigger upgrade*, 2017 *JINST* **12** C01095.

[12] CMS collaboration *Phase 1 upgrade of the CMS drift tubes read-out system*, 2017 *JINST* **12** C03070.

[13] CMS collaboration, *Validation of the mean-timer algorithm for DT local reconstruction and muon time measurement, using 2012 data*, CMS-DP-2015-026, CERN, Geneva, Switzerland, (2015).

[14] CMS collaboration, *Description and performance of track and primary-vertex reconstruction with the CMS tracker*, 2014 *JINST* **9** P10009 [arXiv:1405.6569].

[15] CMS collaboration, *Performance of CMS muon reconstruction in cosmic-ray events*, 2010 *JINST* **5** T03022 [arXiv:0911.4994].

[16] R. Frühwirth, *Application of Kalman filtering to track and vertex fitting*, *Nucl. Instrum. Meth.* **A 262** (1987) 444.

[17] CMS collaboration, *Particle-flow reconstruction and global event description with the CMS detector*, 2017 *JINST* **12** P10003 [arXiv:1706.04965].

[18] CMS collaboration, *Technical proposal for the phase-II upgrade of the CMS detector*, CERN-LHCC-2015-010, CERN, Geneva, Switzerland, (2015) [CMS-TDR-15-02].

[19] J. Alwall et al., *The automated computation of tree-level and next-to-leading order differential cross sections and their matching to parton shower simulations*, *JHEP* **07** (2014) 079 [arXiv:1405.0301].

[20] E. Re, *Single-top Wt-channel production matched with parton showers using the POWHEG method*, *Eur. Phys. J.* **C 71** (2011) 1547 [arXiv:1009.2450].

[21] T. Sjöstrand, S. Mrenna and P.Z. Skands, *PYTHIA 6.4 physics and manual*, *JHEP* **05** (2006) 026 [hep-ph/0603175].

[22] T. Sjöstrand et al., *An introduction to PYTHIA 8.2*, *Comput. Phys. Commun.* **191** (2015) 159 [arXiv:1410.3012].

[23] CMS collaboration, *Event generator tunes obtained from underlying event and multiparton scattering measurements*, *Eur. Phys. J.* **C 76** (2016) 155 [arXiv:1512.00815].

[24] NNPDF collaboration, R.D. Ball et al., *Parton distributions for the LHC run II*, *JHEP* **04** (2015) 040 [arXiv:1410.8849].

[25] GEANT4 collaboration, S. Agostinelli et al., *GEANT4: a simulation toolkit*, *Nucl. Instrum. Meth.* **A 506** (2003) 250.

[26] A.C. Rencher and G.B. Schaalje, *Linear models in statistics*, John Wiley & Sons Inc., New York, U.S.A., (2008).

[27] CMS collaboration, *Alignment of the CMS tracker with LHC and cosmic ray data*, 2014 *JINST* **9** P06009 [arXiv:1403.2286].

[28] CMS collaboration, *CMS technical design report, volume II: physics performance*, *J. Phys.* **G 34** (2007) 995.

2018 JINST 13 P06015

[29] A. Bodek, A. van Dyne, J.Y. Han, W. Sakumoto and A. Strelnikov, *Extracting muon momentum scale corrections for hadron collider experiments*, *Eur. Phys. J.* **C 72** (2012) 2194 [arXiv:1208.3710].

[30] CMS collaboration, *W-like measurement of the Z boson mass using dimuon events collected in pp collisions at* $\sqrt{s} = 7$ *TeV*, CMS-PAS-SMP-14-007, CERN, Geneva, Switzerland, (2014).

[31] CMS collaboration, *Search for heavy long-lived charged particles in pp collisions at* $\sqrt{s} = 7$ *TeV*, *Phys. Lett.* **B 713** (2012) 408 [arXiv:1205.0272].

[32] M. Cacciari, G.P. Salam and G. Soyez, *FastJet user manual*, *Eur. Phys. J.* **C 72** (2012) 1896 [arXiv:1111.6097].

[33] M. Abbrescia et al., *Beam test results on double-gap resistive plate chambers proposed for CMS experiment*, *Nucl. Instrum. Meth.* **A 414** (1998) 135.

[34] CMS collaboration, *Measurement of inclusive W and Z boson production cross sections in pp collisions at* $\sqrt{s} = 8$ *TeV*, *Phys. Rev. Lett.* **112** (2014) 191802 [arXiv:1402.0923].

[35] CMS collaboration, *Measurement of inclusive W and Z boson production cross sections in pp collisions at* $\sqrt{s} = 13$ *TeV*, CMS-PAS-SMP-15-004, CERN, Geneva, Switzerland, (2015).

2018 JINST 13 P06015

The CMS collaboration

Yerevan Physics Institute, Yerevan, Armenia

A.M. Sirunyan, A. Tumasyan

Institut für Hochenergiephysik, Wien, Austria

W. Adam, F. Ambrogi, E. Asilar, T. Bergauer, J. Brandstetter, E. Brondolin, M. Dragicevic, J. Erö, A. Escalante Del Valle, M. Flechl, M. Friedl, R. Frühwirth[1], V.M. Ghete, J. Grossmann, J. Hrubec, M. Jeitler[1], A. König, N. Krammer, I. Krätschmer, D. Liko, T. Madlener, I. Mikulec, E. Pree, N. Rad, H. Rohringer, J. Schieck[1], R. Schöfbeck, M. Spanring, D. Spitzbart, A. Taurok, W. Waltenberger, J. Wittmann, C.-E. Wulz[1], M. Zarucki

Institute for Nuclear Problems, Minsk, Belarus

V. Chekhovsky, V. Mossolov, J. Suarez Gonzalez

Universiteit Antwerpen, Antwerpen, Belgium

E.A. De Wolf, D. Di Croce, X. Janssen, J. Lauwers, M. Van De Klundert, H. Van Haevermaet, P. Van Mechelen, N. Van Remortel

Vrije Universiteit Brussel, Brussel, Belgium

S. Abu Zeid, F. Blekman, J. D'Hondt, I. De Bruyn, J. De Clercq, K. Deroover, G. Flouris, D. Lontkovskyi, S. Lowette, I. Marchesini, S. Moortgat, L. Moreels, Q. Python, K. Skovpen, S. Tavernier, W. Van Doninck, P. Van Mulders, I. Van Parijs

Université Libre de Bruxelles, Bruxelles, Belgium

D. Beghin, B. Bilin, H. Brun, B. Clerbaux, G. De Lentdecker, H. Delannoy, B. Dorney, G. Fasanella, L. Favart, R. Goldouzian, A. Grebenyuk, A.K. Kalsi, T. Lenzi, J. Luetic, T. Maerschalk, A. Marinov, T. Seva, E. Starling, C. Vander Velde, P. Vanlaer, D. Vannerom, R. Yonamine, F. Zenoni

Ghent University, Ghent, Belgium

T. Cornelis, D. Dobur, A. Fagot, M. Gul, I. Khvastunov[2], D. Poyraz, C. Roskas, S. Salva, D. Trocino, M. Tytgat, W. Verbeke, M. Vit, N. Zaganidis

Université Catholique de Louvain, Louvain-la-Neuve, Belgium

H. Bakhshiansohi, O. Bondu, S. Brochet, G. Bruno, C. Caputo, A. Caudron, P. David, S. De Visscher, C. Delaere, M. Delcourt, B. Francois, A. Giammanco, M. Komm, G. Krintiras, V. Lemaitre, A. Magitteri, A. Mertens, M. Musich, K. Piotrzkowski, L. Quertenmont, A. Saggio, M. Vidal Marono, S. Wertz, J. Zobec

Centro Brasileiro de Pesquisas Fisicas, Rio de Janeiro, Brazil

W.L. Aldá Júnior, F.L. Alves, G.A. Alves, L. Brito, G. Correia Silva, C. Hensel, A. Moraes, M.E. Pol, P. Rebello Teles

Universidade do Estado do Rio de Janeiro, Rio de Janeiro, Brazil

E. Belchior Batista Das Chagas, W. Carvalho, J. Chinellato[3], E. Coelho, E.M. Da Costa, G.G. Da Silveira[4], D. De Jesus Damiao, S. Fonseca De Souza, L.M. Huertas Guativa, H. Malbouisson, M. Melo De Almeida, C. Mora Herrera, L. Mundim, H. Nogima, L.J. Sanchez Rosas,

2018 JINST 13 P06015

A. Santoro, A. Sznajder, M. Thiel, E.J. Tonelli Manganote[3], F. Torres Da Silva De Araujo, A. Vilela Pereira

Universidade Estadual Paulista [a], Universidade Federal do ABC [b], São Paulo, Brazil
S. Ahuja[a], C.A. Bernardes[a], T.R. Fernandez Perez Tomei[a], E.M. Gregores[b], P.G. Mercadante[b], S.F. Novaes[a], Sandra S. Padula[a], D. Romero Abad[b], J.C. Ruiz Vargas[a]

Institute for Nuclear Research and Nuclear Energy, Bulgarian Academy of Sciences, Sofia, Bulgaria
A. Aleksandrov, R. Hadjiiska, P. Iaydjiev, M. Misheva, M. Rodozov, M. Shopova, G. Sultanov

University of Sofia, Sofia, Bulgaria
A. Dimitrov, L. Litov, B. Pavlov, P. Petkov

Beihang University, Beijing, China
W. Fang[5], X. Gao[5], L. Yuan

Institute of High Energy Physics, Beijing, China
M. Ahmad, J.G. Bian, G.M. Chen, H.S. Chen, M. Chen, Y. Chen, C.H. Jiang, D. Leggat, H. Liao, Z. Liu, F. Romeo, S.M. Shaheen, A. Spiezia, J. Tao, C. Wang, Z. Wang, E. Yazgan, H. Zhang, J. Zhao

State Key Laboratory of Nuclear Physics and Technology, Peking University, Beijing, China
Y. Ban, G. Chen, J. Li, Q. Li, S. Liu, Y. Mao, S.J. Qian, D. Wang, Z. Xu, F. Zhang[5]

Tsinghua University, Beijing, China
Y. Wang

Universidad de Los Andes, Bogota, Colombia
C. Avila, A. Cabrera, C.A. Carrillo Montoya, L.F. Chaparro Sierra, C. Florez, C.F. González Hernández, J.D. Ruiz Alvarez, M.A. Segura Delgado

University of Split, Faculty of Electrical Engineering, Mechanical Engineering and Naval Architecture, Split, Croatia
B. Courbon, N. Godinovic, D. Lelas, I. Puljak, P.M. Ribeiro Cipriano, T. Sculac

University of Split, Faculty of Science, Split, Croatia
Z. Antunovic, M. Kovac

Institute Rudjer Boskovic, Zagreb, Croatia
V. Brigljevic, D. Ferencek, K. Kadija, B. Mesic, A. Starodumov[6], T. Susa

University of Cyprus, Nicosia, Cyprus
M.W. Ather, A. Attikis, G. Mavromanolakis, J. Mousa, C. Nicolaou, F. Ptochos, P.A. Razis, H. Rykaczewski

Charles University, Prague, Czech Republic
M. Finger[7], M. Finger Jr.[7]

Universidad San Francisco de Quito, Quito, Ecuador
E. Carrera Jarrin

2018 JINST 13 P06015

Academy of Scientific Research and Technology of the Arab Republic of Egypt, Egyptian Network of High Energy Physics, Cairo, Egypt
H. Abdalla[8], Y. Assran[9,10], A. Mohamed[11]

National Institute of Chemical Physics and Biophysics, Tallinn, Estonia
S. Bhowmik, R.K. Dewanjee, M. Kadastik, L. Perrini, M. Raidal, C. Veelken

Department of Physics, University of Helsinki, Helsinki, Finland
P. Eerola, H. Kirschenmann, J. Pekkanen, M. Voutilainen

Helsinki Institute of Physics, Helsinki, Finland
J. Havukainen, J.K. Heikkilä, T. Järvinen, V. Karimäki, R. Kinnunen, T. Lampén, K. Lassila-Perini, S. Laurila, S. Lehti, T. Lindén, P. Luukka, T. Mäenpää, H. Siikonen, E. Tuominen, J. Tuominiemi

Lappeenranta University of Technology, Lappeenranta, Finland
T. Tuuva

IRFU, CEA, Université Paris-Saclay, Gif-sur-Yvette, France
M. Besancon, F. Couderc, M. Dejardin, D. Denegri, J.L. Faure, F. Ferri, S. Ganjour, S. Ghosh, A. Givernaud, P. Gras, G. Hamel de Monchenault, P. Jarry, C. Leloup, E. Locci, M. Machet, J. Malcles, G. Negro, J. Rander, A. Rosowsky, M.Ö. Sahin, M. Titov

Laboratoire Leprince-Ringuet, Ecole polytechnique, CNRS/IN2P3, Université Paris-Saclay, Palaiseau, France
A. Abdulsalam[12], C. Amendola, I. Antropov, S. Baffioni, F. Beaudette, P. Busson, L. Cadamuro, C. Charlot, R. Granier de Cassagnac, M. Jo, I. Kucher, S. Lisniak, A. Lobanov, J. Martin Blanco, M. Nguyen, C. Ochando, G. Ortona, P. Paganini, P. Pigard, R. Salerno, J.B. Sauvan, Y. Sirois, A.G. Stahl Leiton, T. Strebler, Y. Yilmaz, A. Zabi, A. Zghiche

Université de Strasbourg, CNRS, IPHC, Strasbourg, France
J.-L. Agram[13], J. Andrea, D. Bloch, J.-M. Brom, M. Buttignol, E.C. Chabert, N. Chanon, C. Collard, E. Conte[13], X. Coubez, F. Drouhin[13], J.-C. Fontaine[13], D. Gelé, U. Goerlach, M. Jansová, P. Juillot, A.-C. Le Bihan, N. Tonon, P. Van Hove

Centre de Calcul de l'Institut National de Physique Nucleaire et de Physique des Particules, CNRS/IN2P3, Villeurbanne, France
S. Gadrat

Université de Lyon, Université Claude Bernard Lyon 1, CNRS-IN2P3, Institut de Physique Nucléaire de Lyon, Villeurbanne, France
S. Beauceron, C. Bernet, G. Boudoul, R. Chierici, D. Contardo, P. Depasse, H. El Mamouni, J. Fay, L. Finco, S. Gascon, M. Gouzevitch, G. Grenier, B. Ille, F. Lagarde, I.B. Laktineh, M. Lethuillier, L. Mirabito, A.L. Pequegnot, S. Perries, A. Popov[14], V. Sordini, M. Vander Donckt, S. Viret, S. Zhang

Georgian Technical University, Tbilisi, Georgia
I. Lomidze, T. Toriashvili[15]

2018 JINST 13 P06015

Tbilisi State University, Tbilisi, Georgia
I. Bagaturia[16], D. Lomidze

RWTH Aachen University, I. Physikalisches Institut, Aachen, Germany
C. Autermann, L. Feld, M.K. Kiesel, K. Klein, M. Lipinski, M. Preuten, C. Schomakers, J. Schulz, M. Teroerde, B. Wittmer, V. Zhukov[14]

RWTH Aachen University, III. Physikalisches Institut A, Aachen, Germany
A. Albert, D. Duchardt, M. Endres, M. Erdmann, S. Erdweg, T. Esch, R. Fischer, A. Güth, T. Hebbeker, C. Heidemann, K. Hoepfner, S. Knutzen, M. Merschmeyer, A. Meyer, P. Millet, S. Mukherjee, B. Philipps, T. Pook, M. Radziej, H. Reithler, M. Rieger, F. Scheuch, D. Teyssier, S. Thüer, F.P. Zantis

RWTH Aachen University, III. Physikalisches Institut B, Aachen, Germany
G. Flügge, B. Kargoll, T. Kress, A. Künsken, T. Müller, A. Nehrkorn, A. Nowack, C. Pistone, O. Pooth, A. Stahl[17]

Deutsches Elektronen-Synchrotron, Hamburg, Germany
M. Aldaya Martin, T. Arndt, C. Asawatangtrakuldee, K. Beernaert, O. Behnke, U. Behrens, A. Bermúdez Martínez, A.A. Bin Anuar, K. Borras[18], V. Botta, A. Campbell, P. Connor, C. Contreras-Campana, F. Costanza, C. Diez Pardos, G. Eckerlin, D. Eckstein, T. Eichhorn, E. Eren, E. Gallo[19], J. Garay Garcia, A. Geiser, J.M. Grados Luyando, A. Grohsjean, P. Gunnellini, M. Guthoff, A. Harb, J. Hauk, M. Hempel[20], H. Jung, M. Kasemann, J. Keaveney, C. Kleinwort, I. Korol, D. Krücker, W. Lange, A. Lelek, T. Lenz, K. Lipka, W. Lohmann[20], R. Mankel, I.-A. Melzer-Pellmann, A.B. Meyer, M. Missiroli, G. Mittag, J. Mnich, A. Mussgiller, E. Ntomari, D. Pitzl, A. Raspereza, M. Savitskyi, P. Saxena, R. Shevchenko, N. Stefaniuk, G.P. Van Onsem, R. Walsh, Y. Wen, K. Wichmann, C. Wissing, O. Zenaiev

University of Hamburg, Hamburg, Germany
R. Aggleton, S. Bein, V. Blobel, M. Centis Vignali, T. Dreyer, E. Garutti, D. Gonzalez, J. Haller, A. Hinzmann, M. Hoffmann, A. Karavdina, R. Klanner, R. Kogler, N. Kovalchuk, S. Kurz, D. Marconi, M. Meyer, M. Niedziela, D. Nowatschin, F. Pantaleo[17], T. Peiffer, A. Perieanu, C. Scharf, P. Schleper, A. Schmidt, S. Schumann, J. Schwandt, J. Sonneveld, H. Stadie, G. Steinbrück, F.M. Stober, M. Stöver, H. Tholen, D. Troendle, E. Usai, A. Vanhoefer, B. Vormwald

Institut für Experimentelle Teilchenphysik, Karlsruhe, Germany
M. Akbiyik, C. Barth, M. Baselga, S. Baur, E. Butz, R. Caspart, T. Chwalek, F. Colombo, W. De Boer, A. Dierlamm, N. Faltermann, B. Freund, R. Friese, M. Giffels, M.A. Harrendorf, F. Hartmann[17], S.M. Heindl, U. Husemann, F. Kassel[17], S. Kudella, H. Mildner, M.U. Mozer, Th. Müller, M. Plagge, G. Quast, K. Rabbertz, M. Schröder, I. Shvetsov, G. Sieber, H.J. Simonis, R. Ulrich, S. Wayand, M. Weber, T. Weiler, S. Williamson, C. Wöhrmann, R. Wolf

Institute of Nuclear and Particle Physics (INPP), NCSR Demokritos, Aghia Paraskevi, Greece
G. Anagnostou, G. Daskalakis, T. Geralis, A. Kyriakis, D. Loukas, I. Topsis-Giotis

National and Kapodistrian University of Athens, Athens, Greece
G. Karathanasis, S. Kesisoglou, A. Panagiotou, N. Saoulidou, E. Tziaferi

2018 JINST 13 P06015

National Technical University of Athens, Athens, Greece

K. Kousouris

University of Ioánnina, Ioánnina, Greece

I. Evangelou, C. Foudas, P. Gianneios, P. Katsoulis, P. Kokkas, S. Mallios, N. Manthos, I. Papadopoulos, E. Paradas, J. Strologas, F.A. Triantis, D. Tsitsonis

MTA-ELTE Lendület CMS Particle and Nuclear Physics Group, Eötvös Loránd University, Budapest, Hungary

M. Csanad, N. Filipovic, G. Pasztor, O. Surányi, G.I. Veres[21]

Wigner Research Centre for Physics, Budapest, Hungary

G. Bencze, C. Hajdu, D. Horvath[22], Á. Hunyadi, F. Sikler, V. Veszpremi, G. Vesztergombi[21]

Institute of Nuclear Research ATOMKI, Debrecen, Hungary

N. Beni, S. Czellar, J. Karancsi[23], A. Makovec, J. Molnar, Z. Szillasi

Institute of Physics, University of Debrecen, Debrecen, Hungary

M. Bartók[21], P. Raics, Z.L. Trocsanyi, B. Ujvari

Indian Institute of Science (IISc), Bangalore, India

S. Choudhury, J.R. Komaragiri

National Institute of Science Education and Research, Bhubaneswar, India

S. Bahinipati[24], P. Mal, K. Mandal, A. Nayak[25], D.K. Sahoo[24], N. Sahoo, S.K. Swain

Panjab University, Chandigarh, India

S. Bansal, S.B. Beri, V. Bhatnagar, R. Chawla, N. Dhingra, A. Kaur, M. Kaur, S. Kaur, R. Kumar, P. Kumari, A. Mehta, J.B. Singh, G. Walia

University of Delhi, Delhi, India

A. Bhardwaj, S. Chauhan, B.C. Choudhary, R.B. Garg, S. Keshri, A. Kumar, Ashok Kumar, S. Malhotra, M. Naimuddin, K. Ranjan, Aashaq Shah, R. Sharma

Saha Institute of Nuclear Physics, HBNI, Kolkata, India

R. Bhardwaj[26], R. Bhattacharya, S. Bhattacharya, U. Bhawandeep[26], D. Bhowmik, S. Dey, S. Dutt[26], S. Dutta, S. Ghosh, N. Majumdar, A. Modak, K. Mondal, S. Mukhopadhyay, S. Nandan, A. Purohit, P.K. Rout, A. Roy, S. Roy Chowdhury, S. Sarkar, M. Sharan, B. Singh, S. Thakur[26]

Indian Institute of Technology Madras, Madras, India

P.K. Behera

Bhabha Atomic Research Centre, Mumbai, India

R. Chudasama, D. Dutta, V. Jha, V. Kumar, A.K. Mohanty[17], P.K. Netrakanti, L.M. Pant, P. Shukla, A. Topkar

Tata Institute of Fundamental Research-A, Mumbai, India

T. Aziz, S. Dugad, B. Mahakud, S. Mitra, G.B. Mohanty, N. Sur, B. Sutar

2018 JINST 13 P06015

Tata Institute of Fundamental Research-B, Mumbai, India

S. Banerjee, S. Bhattacharya, S. Chatterjee, P. Das, M. Guchait, Sa. Jain, S. Kumar, M. Maity[27], G. Majumder, K. Mazumdar, T. Sarkar[27], N. Wickramage[28]

Indian Institute of Science Education and Research (IISER), Pune, India

S. Chauhan, S. Dube, V. Hegde, A. Kapoor, K. Kothekar, S. Pandey, A. Rane, S. Sharma

Institute for Research in Fundamental Sciences (IPM), Tehran, Iran

S. Chenarani[29], E. Eskandari Tadavani, S.M. Etesami[29], M. Khakzad, M. Mohammadi Najafabadi, M. Naseri, S. Paktinat Mehdiabadi[30], F. Rezaei Hosseinabadi, B. Safarzadeh[31], M. Zeinali

University College Dublin, Dublin, Ireland

M. Felcini, M. Grunewald

INFN Sezione di Bari (a, Università di Bari (b, Politecnico di Bari [c], Bari, Italy

M. Abbrescia[a,b], C. Calabria[a,b], A. Colaleo[a], D. Creanza[a,c], L. Cristella[a,b], N. De Filippis[a,c], M. De Palma[a,b], F. Errico[a,b], L. Fiore[a], M. Franco[a], G. Iaselli[a,c], N. Lacalamita[a], S. Lezki[a,b], G. Maggi[a,c], M. Maggi[a], S. Martiradonna[a,b], G. Miniello[a,b], S. My[a,b], S. Nuzzo[a,b], A. Pompili[a,b], G. Pugliese[a,c], R. Radogna[a], A. Ranieri[a], G. Selvaggi[a,b], A. Sharma[a], L. Silvestris[a,17], R. Venditti[a], P. Verwilligen[a]

INFN Sezione di Bologna (a, Università di Bologna [b], Bologna, Italy

G. Abbiendi[a], G. Balbi, C. Baldanza[a], C. Battilana[a,b], D. Bonacorsi[a,b], L. Borgonovi[a,b], S. Braibant-Giacomelli[a,b], V.D. Cafaro[a], R. Campanini[a,b], P. Capiluppi[a,b], A. Castro[a,b], F.R. Cavallo[a], S.S. Chhibra[a,b], G. Codispoti[a,b], M. Cuffiani[a,b], G.M. Dallavalle[a], F. Fabbri[a], A. Fanfani[a,b], D. Fasanella[a,b], P. Giacomelli[a], V. Giordano[a], C. Grandi[a], L. Guiducci[a,b], F. Iemmi, S. Marcellini[a], G. Masetti[a], A. Montanari[a], F.L. Navarria[a,b], A. Perrotta[a], A.M. Rossi[a,b], T. Rovelli[a,b], G.P. Siroli[a,b], N. Tosi[a], R. Travaglini[a,b]

INFN Sezione di Catania (a, Università di Catania [b], Catania, Italy

S. Albergo[a,b], S. Costa[a,b], A. Di Mattia[a], F. Giordano[a,b], R. Potenza[a,b], A. Tricomi[a,b], C. Tuve[a,b]

INFN Sezione di Firenze (a, Università di Firenze [b], Firenze, Italy

G. Barbagli[a], K. Chatterjee[a,b], V. Ciulli[a,b], C. Civinini[a], R. D'Alessandro[a,b], E. Focardi[a,b], P. Lenzi[a,b], M. Meschini[a], S. Paoletti[a], L. Russo[a,32], G. Sguazzoni[a], D. Strom[a], L. Viliani[a]

INFN Laboratori Nazionali di Frascati, Frascati, Italy

L. Benussi, S. Bianco, M. Caponero[33], F. Fabbri, M. Ferrini, L. Passamonti, D. Piccolo, D. Pierluigi, F. Primavera[17], A. Russo, G. Saviano[34]

INFN Sezione di Genova (a, Università di Genova [b], Genova, Italy

V. Calvelli[a,b], F. Ferro[a], F. Ravera[a,b], E. Robutti[a], S. Tosi[a,b]

INFN Sezione di Milano-Bicocca (a, Università di Milano-Bicocca [b], Milano, Italy

A. Benaglia[a], A. Beschi[b], L. Brianza[a,b], F. Brivio[a,b], V. Ciriolo[a,b,17], M.E. Dinardo[a,b], S. Fiorendi[a,b], S. Gennai[a], A. Ghezzi[a,b], P. Govoni[a,b], M. Malberti[a,b], S. Malvezzi[a], R.A. Manzoni[a,b], D. Menasce[a], L. Moroni[a], M. Paganoni[a,b], K. Pauwels[a,b], D. Pedrini[a], S. Pigazzini[a,b,35], S. Ragazzi[a,b], T. Tabarelli de Fatis[a,b]

2018 JINST 13 P06015

INFN Sezione di Napoli (a, Università di Napoli 'Federico II' (b, Napoli, Italy, Università della Basilicata (c, Potenza, Italy, Università G. Marconi (d, Roma, Italy

S. Buontempo, N. Cavallo, S. Di Guida[17], F. Fabozzi, F. Fienga, A.O.M. Iorio, W.A. Khan, L. Lista, S. Meola[17], P. Paolucci[17], C. Sciacca, F. Thyssen

INFN Sezione di Padova (a, Università di Padova (b, Padova, Italy, Università di Trento (c, Trento, Italy

P. Azzi, N. Bacchetta, L. Barcellan, M. Bellato, L. Benato, M. Benettoni, M. Biasotto[36], D. Bisello, A. Boletti, A. Branca, R. Carlin, P. Checchia, L. Ciano, M. Dall'Osso, P. De Castro Manzano, T. Dorigo, U. Dosselli, S. Fantinel, F. Fanzago, F. Gasparini, U. Gasparini, F. Gonella, A. Gozzelino, M. Gulmini[36], R. Isocrate, S. Lacaprara, M. Margoni, A.T. Meneguzzo, G. Mocellin, F. Montecassiano, M. Passaseo, M. Pegoraro, N. Pozzobon, P. Ronchese, R. Rossin, M. Sgaravatto, F. Simonetto, A. Tiko, N. Toniolo, E. Torassa, S. Ventura, M. Zanetti, P. Zotto, G. Zumerle

INFN Sezione di Pavia (a, Università di Pavia [b], Pavia, Italy

A. Braghieri[a], A. Magnani[a], P. Montagna[a,b], S.P. Ratti[a,b], V. Re[a], M. Ressegotti[a,b], C. Riccardi[a,b], P. Salvini[a], I. Vai[a,b], P. Vitulo[a,b]

INFN Sezione di Perugia (a, Università di Perugia [b], Perugia, Italy

L. Alunni Solestizi[a,b], M. Biasini[a,b], G.M. Bilei[a], C. Cecchi[a,b], D. Ciangottini[a,b], L. Fanò[a,b], P. Lariccia[a,b], R. Leonardi[a,b], E. Manoni[a], G. Mantovani[a,b], V. Mariani[a,b], M. Menichelli[a], A. Rossi[a,b], A. Santocchia[a,b], D. Spiga[a]

INFN Sezione di Pisa (a, Università di Pisa (b, Scuola Normale Superiore di Pisa [c], Pisa, Italy

K. Androsov[a], P. Azzurri[a,17], G. Bagliesi[a], L. Bianchini[a], T. Boccali[a], L. Borrello, R. Castaldi[a], M.A. Ciocci[a,b], R. Dell'Orso[a], G. Fedi[a], L. Giannini[a,c], A. Giassi[a], M.T. Grippo[a,32], F. Ligabue[a,c], T. Lomtadze[a], E. Manca[a,c], G. Mandorli[a,c], A. Messineo[a,b], F. Palla[a], A. Rizzi[a,b], A. Savoy-Navarro[a,37], P. Spagnolo[a], R. Tenchini[a], G. Tonelli[a,b], A. Venturi[a], P.G. Verdini[a]

INFN Sezione di Roma (a, Sapienza Università di Roma [b], Rome, Italy

L. Barone[a,b], F. Cavallari[a], M. Cipriani[a,b], N. Daci[a], D. Del Re[a,b], E. Di Marco[a,b], M. Diemoz[a], S. Gelli[a,b], E. Longo[a,b], F. Margaroli[a,b], B. Marzocchi[a,b], P. Meridiani[a], G. Organtini[a,b], R. Paramatti[a,b], F. Preiato[a,b], S. Rahatlou[a,b], C. Rovelli[a], F. Santanastasio[a,b]

INFN Sezione di Torino (a, Università di Torino (b, Torino, Italy, Università del Piemonte Orientale (c, Novara, Italy

N. Amapane, R. Arcidiacono, S. Argiro, M. Arneodo, N. Bartosik, R. Bellan, C. Biino, N. Cartiglia, F. Cenna, M. Costa, G. Cotto, R. Covarelli, D. Dattola, P. De Remigis, G. Dellacasa, N. Demaria, B. Kiani, C. Mariotti, S. Maselli, G. Mazza, E. Migliore, V. Monaco, E. Monteil, M. Monteno, M.M. Obertino, L. Pacher, N. Pastrone, M. Pelliccioni, G.L. Pinna Angioni, F. Rotondo, M. Ruspa, R. Sacchi, K. Shchelina, V. Sola, A. Solano, A. Staiano, P. Traczyk

INFN Sezione di Trieste (a, Università di Trieste [b], Trieste, Italy

S. Belforte[a], M. Casarsa[a], F. Cossutti[a], G. Della Ricca[a,b], A. Zanetti[a]

2018 JINST 13 P06015

Kyungpook National University
D.H. Kim, G.N. Kim, M.S. Kim, J. Lee, S. Lee, S.W. Lee, C.S. Moon, Y.D. Oh, S. Sekmen, D.C. Son, Y.C. Yang

Chonnam National University, Institute for Universe and Elementary Particles, Kwangju, Korea
H. Kim, D.H. Moon, G. Oh

Hanyang University, Seoul, Korea
J.A. Brochero Cifuentes, J. Goh, T.J. Kim

Korea University, Seoul, Korea
S. Cho, S. Choi, Y. Go, D. Gyun, S. Ha, B. Hong, Y. Jo, Y. Kim, K. Lee, K.S. Lee, S. Lee, J. Lim, S.K. Park, Y. Roh

Seoul National University, Seoul, Korea
J. Almond, J. Kim, J.S. Kim, H. Lee, K. Lee, K. Nam, S.B. Oh, B.C. Radburn-Smith, S.h. Seo, U.K. Yang, H.D. Yoo, G.B. Yu

University of Seoul, Seoul, Korea
H. Kim, J.H. Kim, J.S.H. Lee, I.C. Park

Sungkyunkwan University, Suwon, Korea
Y. Choi, C. Hwang, J. Lee, I. Yu

Vilnius University, Vilnius, Lithuania
V. Dudenas, A. Juodagalvis, J. Vaitkus

National Centre for Particle Physics, Universiti Malaya, Kuala Lumpur, Malaysia
I. Ahmed, Z.A. Ibrahim, M.A.B. Md Ali[38], F. Mohamad Idris[39], W.A.T. Wan Abdullah, M.N. Yusli, Z. Zolkapli

Centro de Investigacion y de Estudios Avanzados del IPN, Mexico City, Mexico
Duran-Osuna, M. C., H. Castilla-Valdez, E. De La Cruz-Burelo, Ramirez-Sanchez, G., I. Heredia-De La Cruz[40], Rabadan-Trejo, R. I., R. Lopez-Fernandez, J. Mejia Guisao, Reyes-Almanza, R, A. Sanchez-Hernandez

Universidad Iberoamericana, Mexico City, Mexico
S. Carrillo Moreno, C. Oropeza Barrera, F. Vazquez Valencia

Benemerita Universidad Autonoma de Puebla, Puebla, Mexico
J. Eysermans, I. Pedraza, H.A. Salazar Ibarguen, C. Uribe Estrada

Universidad Autónoma de San Luis Potosí, San Luis Potosí, Mexico
A. Morelos Pineda

University of Auckland, Auckland, New Zealand
D. Krofcheck

University of Canterbury, Christchurch, New Zealand
S. Bheesette, P.H. Butler

2018 JINST 13 P06015

National Centre for Physics, Quaid-I-Azam University, Islamabad, Pakistan
A. Ahmad, M. Ahmad, M.I. Asghar, Q. Hassan, H.R. Hoorani, M.A. Shah, M. Shoaib, M. Waqas

National Centre for Nuclear Research, Swierk, Poland
H. Bialkowska, M. Bluj, B. Boimska, T. Frueboes, M. Górski, M. Kazana, K. Nawrocki, M. Szleper, P. Zalewski

Institute of Experimental Physics, Faculty of Physics, University of Warsaw, Warsaw, Poland
K. Bunkowski, A. Byszuk[41], K. Doroba, A. Kalinowski, M. Konecki, J. Krolikowski, M. Misiura, M. Olszewski, A. Pyskir, M. Walczak

Laboratório de Instrumentação e Física Experimental de Partículas, Lisboa, Portugal
P. Bargassa, C. Beirão Da Cruz E Silva, A. Di Francesco, P. Faccioli, B. Galinhas, M. Gallinaro, J. Hollar, N. Leonardo, L. Lloret Iglesias, M.V. Nemallapudi, J. Seixas, G. Strong, O. Toldaiev, D. Vadruccio, J. Varela

Joint Institute for Nuclear Research, Dubna, Russia
S. Afanasiev, P. Bunin, Y. Ershov, A. Evdokimov, M. Gavrilenko, A. Golunov, I. Golutvin, I. Gorbunov, A. Kamenev, V. Karjavine, A. Kurenkov, A. Lanev, A. Makankin, A. Malakhov, V. Matveev[42,43], P. Moisenz, V. Palichik, V. Perelygin, S. Shmatov, S. Shulha, N. Skatchkov, V. Smirnov, S. Vasil'ev, N. Voytishin, A. Zarubin

Petersburg Nuclear Physics Institute, Gatchina (St. Petersburg), Russia
Y. Ivanov, V. Kim[44], E. Kuznetsova[45], P. Levchenko, V. Murzin, V. Oreshkin, I. Smirnov, D. Sosnov, V. Sulimov, L. Uvarov, S. Vavilov, A. Vorobyev

Institute for Nuclear Research, Moscow, Russia
Yu. Andreev, A. Dermenev, S. Gninenko, N. Golubev, A. Karneyeu, M. Kirsanov, N. Krasnikov, A. Pashenkov, D. Tlisov, A. Toropin

Institute for Theoretical and Experimental Physics, Moscow, Russia
V. Epshteyn, V. Gavrilov, N. Lychkovskaya, V. Popov, I. Pozdnyakov, G. Safronov, A. Spiridonov, A. Stepennov, V. Stolin, M. Toms, E. Vlasov, A. Zhokin

Moscow Institute of Physics and Technology, Moscow, Russia
T. Aushev, A. Bylinkin[43]

National Research Nuclear University 'Moscow Engineering Physics Institute' (MEPhI), Moscow, Russia
S. Polikarpov

P.N. Lebedev Physical Institute, Moscow, Russia
V. Andreev, M. Azarkin[43], I. Dremin[43], M. Kirakosyan[43], S.V. Rusakov, A. Terkulov

Skobeltsyn Institute of Nuclear Physics, Lomonosov Moscow State University, Moscow, Russia
A. Baskakov, A. Belyaev, G. Bogdanova, E. Boos, L. Dudko, A. Ershov, A. Gribushin, V. Klyukhin, O. Kodolova, I. Lokhtin, I. Miagkov, S. Obraztsov, S. Petrushanko, V. Savrin, V. Volkov

Novosibirsk State University (NSU), Novosibirsk, Russia
V. Blinov[46], D. Shtol[46], Y. Skovpen[46]

2018 JINST 13 P06015

State Research Center of Russian Federation, Institute for High Energy Physics of NRC "Kurchatov Institute", Protvino, Russia

I. Azhgirey, I. Bayshev, S. Bitioukov, D. Elumakhov, A. Godizov, V. Kachanov, A. Kalinin, D. Konstantinov, P. Mandrik, V. Petrov, R. Ryutin, A. Sobol, S. Troshin, N. Tyurin, A. Uzunian, A. Volkov

University of Belgrade, Faculty of Physics and Vinca Institute of Nuclear Sciences, Belgrade, Serbia

P. Adzic[47], P. Cirkovic, D. Devetak, M. Dordevic, J. Milosevic

Centro de Investigaciones Energéticas Medioambientales y Tecnológicas (CIEMAT), Madrid, Spain

J. Alcaraz Maestre, A. Álvarez Fernández, I. Bachiller, M. Barrio Luna, E. Calvo, J.M. Cela Ruiz, M. Cerrada, N. Colino, B. De La Cruz, A. Delgado Peris, C. Fernandez Bedoya, J.P. Fernández Ramos, J. Flix, M.C. Fouz, D. Francia Ferrero, O. Gonzalez Lopez, S. Goy Lopez, J.M. Hernandez, M.I. Josa, D. Moran, Á. Navarro Tobar, A. Pérez-Calero Yzquierdo, J. Puerta Pelayo, I. Redondo, D.D. Redondo Ferrero, L. Romero, J. Sastre, M.S. Soares, A. Triossi

Universidad Autónoma de Madrid, Madrid, Spain

C. Albajar, J.F. de Trocóniz

Universidad de Oviedo, Oviedo, Spain

J. Cuevas, C. Erice, J. Fernandez Menendez, I. Gonzalez Caballero, J.R. González Fernández, E. Palencia Cortezon, S. Sanchez Cruz, P. Vischia, J.M. Vizan Garcia

Instituto de Física de Cantabria (IFCA), CSIC-Universidad de Cantabria, Santander, Spain

I.J. Cabrillo, A. Calderon, B. Chazin Quero, E. Curras, J. Duarte Campderros, M. Fernandez, P.J. Fernández Manteca, A. García Alonso, J. Garcia-Ferrero, G. Gomez, A. Lopez Virto, J. Marco, C. Martinez Rivero, P. Martinez Ruiz del Arbol, F. Matorras, J. Piedra Gomez, C. Prieels, T. Rodrigo, A. Ruiz-Jimeno, L. Scodellaro, N. Trevisani, I. Vila, R. Vilar Cortabitarte

CERN, European Organization for Nuclear Research, Geneva, Switzerland

D. Abbaneo, B. Akgun, E. Auffray, P. Baillon, A.H. Ball, D. Barney, J. Bendavid, M. Bianco, A. Bocci, C. Botta, T. Camporesi, R. Castello, M. Cepeda, G. Cerminara, E. Chapon, Y. Chen, D. d'Enterria, A. Dabrowski, V. Daponte, A. David, M. De Gruttola, A. De Roeck, N. Deelen, M. Dobson, T. du Pree, M. Dünser, N. Dupont, A. Elliott-Peisert, P. Everaerts, F. Fallavollita, G. Franzoni, J. Fulcher, W. Funk, D. Gigi, A. Gilbert, K. Gill, F. Glege, D. Gulhan, J. Hegeman, V. Innocente, A. Jafari, P. Janot, O. Karacheban[20], J. Kieseler, V. Knünz, A. Kornmayer, M.J. Kortelainen, M. Krammer[1], C. Lange, P. Lecoq, C. Lourenço, M.T. Lucchini, L. Malgeri, M. Mannelli, A. Martelli, F. Meijers, J.A. Merlin, S. Mersi, E. Meschi, P. Milenovic[48], F. Moortgat, M. Mulders, H. Neugebauer, J. Ngadiuba, S. Orfanelli, L. Orsini, L. Pape, E. Perez, M. Peruzzi, A. Petrilli, G. Petrucciani, A. Pfeiffer, M. Pierini, F.M. Pitters, D. Rabady, A. Racz, T. Reis, G. Rolandi[49], M. Rovere, H. Sakulin, C. Schäfer, C. Schwick, M. Seidel, M. Selvaggi, A. Sharma, P. Silva, P. Sphicas[50], A. Stakia, J. Steggemann, M. Stoye, M. Tosi, D. Treille, A. Tsirou, V. Veckalns[51], M. Verweij, W.D. Zeuner

2018 JINST 13 P06015

Paul Scherrer Institut, Villigen, Switzerland
W. Bertl[†], L. Caminada[52], K. Deiters, W. Erdmann, R. Horisberger, Q. Ingram, H.C. Kaestli, D. Kotlinski, U. Langenegger, T. Rohe, S.A. Wiederkehr

ETH Zurich - Institute for Particle Physics and Astrophysics (IPA), Zurich, Switzerland
M. Backhaus, L. Bäni, P. Berger, B. Casal, G. Dissertori, M. Dittmar, M. Donegà, C. Dorfer, C. Grab, C. Heidegger, D. Hits, J. Hoss, G. Kasieczka, T. Klijnsma, W. Lustermann, B. Mangano, M. Marionneau, M.T. Meinhard, D. Meister, F. Micheli, P. Musella, F. Nessi-Tedaldi, F. Pandolfi, J. Pata, F. Pauss, G. Perrin, L. Perrozzi, M. Quittnat, M. Reichmann, D.A. Sanz Becerra, M. Schönenberger, L. Shchutska, V.R. Tavolaro, K. Theofilatos, M.L. Vesterbacka Olsson, R. Wallny, D.H. Zhu

Universität Zürich, Zurich, Switzerland
T.K. Aarrestad, C. Amsler[53], M.F. Canelli, A. De Cosa, R. Del Burgo, S. Donato, C. Galloni, T. Hreus, B. Kilminster, D. Pinna, G. Rauco, P. Robmann, D. Salerno, K. Schweiger, C. Seitz, Y. Takahashi, A. Zucchetta

National Central University, Chung-Li, Taiwan
V. Candelise, Y.H. Chang, K.y. Cheng, T.H. Doan, Sh. Jain, R. Khurana, C.M. Kuo, W. Lin, A. Pozdnyakov, S.S. Yu

National Taiwan University (NTU), Taipei, Taiwan
P. Chang, Y. Chao, K.F. Chen, P.H. Chen, F. Fiori, W.-S. Hou, Y. Hsiung, Arun Kumar, Y.F. Liu, R.-S. Lu, E. Paganis, A. Psallidas, A. Steen, J.f. Tsai

Chulalongkorn University, Faculty of Science, Department of Physics, Bangkok, Thailand
B. Asavapibhop, K. Kovitanggoon, G. Singh, N. Srimanobhas

Çukurova University, Physics Department, Science and Art Faculty, Adana, Turkey
M.N. Bakirci[54], A. Bat, F. Boran, S. Cerci[55], S. Damarseckin, Z.S. Demiroglu, C. Dozen, I. Dumanoglu, S. Girgis, G. Gokbulut, Y. Guler, I. Hos[56], E.E. Kangal[57], O. Kara, A. Kayis Topaksu, U. Kiminsu, M. Oglakci, G. Onengut, K. Ozdemir[58], B. Tali[55], U.G. Tok, S. Turkcapar, I.S. Zorbakir, C. Zorbilmez

Middle East Technical University, Physics Department, Ankara, Turkey
G. Karapinar[59], K. Ocalan[60], M. Yalvac, M. Zeyrek

Bogazici University, Istanbul, Turkey
E. Gülmez, M. Kaya[61], O. Kaya[62], S. Tekten, E.A. Yetkin[63]

Istanbul Technical University, Istanbul, Turkey
M.N. Agaras, S. Atay, A. Cakir, K. Cankocak, Y. Komurcu

Institute for Scintillation Materials of National Academy of Science of Ukraine, Kharkov, Ukraine
B. Grynyov

National Scientific Center, Kharkov Institute of Physics and Technology, Kharkov, Ukraine
L. Levchuk

2018 JINST 13 P06015

University of Bristol, Bristol, United Kingdom

F. Ball, L. Beck, J.J. Brooke, D. Burns, E. Clement, D. Cussans, O. Davignon, H. Flacher, J. Goldstein, G.P. Heath, H.F. Heath, L. Kreczko, D.M. Newbold[64], S. Paramesvaran, T. Sakuma, S. Seif El Nasr-storey, D. Smith, V.J. Smith

Rutherford Appleton Laboratory, Didcot, United Kingdom

K.W. Bell, A. Belyaev[65], C. Brew, R.M. Brown, L. Calligaris, D. Cieri, D.J.A. Cockerill, J.A. Coughlan, K. Harder, S. Harper, J. Linacre, E. Olaiya, D. Petyt, C.H. Shepherd-Themistocleous, A. Thea, I.R. Tomalin, T. Williams, W.J. Womersley

Imperial College, London, United Kingdom

G. Auzinger, R. Bainbridge, P. Bloch, J. Borg, S. Breeze, O. Buchmuller, A. Bundock, S. Casasso, M. Citron, D. Colling, L. Corpe, P. Dauncey, G. Davies, M. Della Negra, R. Di Maria, Y. Haddad, G. Hall, G. Iles, T. James, R. Lane, C. Laner, L. Lyons, A.-M. Magnan, S. Malik, L. Mastrolorenzo, T. Matsushita, J. Nash[66], A. Nikitenko[6], V. Palladino, M. Pesaresi, D.M. Raymond, A. Richards, A. Rose, E. Scott, C. Seez, A. Shtipliyski, S. Summers, A. Tapper, K. Uchida, M. Vazquez Acosta[67], T. Virdee[17], N. Wardle, D. Winterbottom, J. Wright, S.C. Zenz

Brunel University, Uxbridge, United Kingdom

J.E. Cole, P.R. Hobson, A. Khan, P. Kyberd, A. Morton, I.D. Reid, L. Teodorescu, S. Zahid

Baylor University, Waco, U.S.A.

A. Borzou, K. Call, J. Dittmann, K. Hatakeyama, H. Liu, N. Pastika, C. Smith

Catholic University of America, Washington DC, U.S.A.

R. Bartek, A. Dominguez

The University of Alabama, Tuscaloosa, U.S.A.

A. Buccilli, S.I. Cooper, C. Henderson, P. Rumerio, C. West

Boston University, Boston, U.S.A.

D. Arcaro, A. Avetisyan, T. Bose, D. Gastler, D. Rankin, C. Richardson, J. Rohlf, L. Sulak, D. Zou

Brown University, Providence, U.S.A.

G. Benelli, D. Cutts, M. Hadley, J. Hakala, U. Heintz, J.M. Hogan, K.H.M. Kwok, E. Laird, G. Landsberg, J. Lee, Z. Mao, M. Narain, J. Pazzini, S. Piperov, S. Sagir, R. Syarif, D. Yu

University of California, Davis, Davis, U.S.A.

R. Band, C. Brainerd, R. Breedon, D. Burns, M. Calderon De La Barca Sanchez, M. Chertok, J. Conway, R. Conway, P.T. Cox, R. Erbacher, C. Flores, G. Funk, W. Ko, R. Lander, C. Mclean, M. Mulhearn, D. Pellett, J. Pilot, S. Shalhout, M. Shi, J. Smith, D. Stolp, D. Taylor, K. Tos, M. Tripathi, Z. Wang

University of California, Los Angeles, U.S.A.

M. Bachtis, C. Bravo, R. Cousins, A. Dasgupta, A. Florent, J. Hauser, M. Ignatenko, N. Mccoll, S. Regnard, D. Saltzberg, C. Schnaible, V. Valuev

2018 JINST 13 P06015

University of California, Riverside, Riverside, U.S.A.

E. Bouvier, K. Burt, R. Clare, J. Ellison, J.W. Gary, S.M.A. Ghiasi Shirazi, G. Hanson, J. Heilman, G. Karapostoli, E. Kennedy, F. Lacroix, O.R. Long, M. Olmedo Negrete, M.I. Paneva, W. Si, L. Wang, H. Wei, S. Wimpenny, B. R. Yates

University of California, San Diego, La Jolla, U.S.A.

J.G. Branson, S. Cittolin, M. Derdzinski, R. Gerosa, D. Gilbert, B. Hashemi, A. Holzner, D. Klein, G. Kole, V. Krutelyov, J. Letts, M. Masciovecchio, D. Olivito, S. Padhi, M. Pieri, M. Sani, V. Sharma, S. Simon, M. Tadel, A. Vartak, S. Wasserbaech[68], J. Wood, F. Würthwein, A. Yagil, G. Zevi Della Porta

University of California, Santa Barbara - Department of Physics, Santa Barbara, U.S.A.

N. Amin, R. Bhandari, J. Bradmiller-Feld, C. Campagnari, A. Dishaw, V. Dutta, M. Franco Sevilla, L. Gouskos, R. Heller, J. Incandela, A. Ovcharova, H. Qu, J. Richman, D. Stuart, I. Suarez, J. Yoo

California Institute of Technology, Pasadena, U.S.A.

D. Anderson, A. Bornheim, J. Bunn, I. Dutta, J.M. Lawhorn, H.B. Newman, T. Q. Nguyen, C. Pena, M. Spiropulu, J.R. Vlimant, R. Wilkinson, S. Xie, Z. Zhang, R.Y. Zhu

Carnegie Mellon University, Pittsburgh, U.S.A.

M.B. Andrews, T. Ferguson, T. Mudholkar, M. Paulini, J. Russ, M. Sun, H. Vogel, I. Vorobiev, M. Weinberg

University of Colorado Boulder, Boulder, U.S.A.

J.P. Cumalat, W.T. Ford, F. Jensen, A. Johnson, M. Krohn, S. Leontsinis, E. Macdonald, T. Mulholland, K. Stenson, S.R. Wagner

Cornell University, Ithaca, U.S.A.

J. Alexander, J. Chaves, Y. Cheng, J. Chu, S. Dittmer, K. Mcdermott, N. Mirman, J.R. Patterson, D. Quach, A. Rinkevicius, A. Ryd, L. Skinnari, L. Soffi, S.M. Tan, Z. Tao, J. Thom, J. Tucker, P. Wittich, M. Zientek

Fermi National Accelerator Laboratory, Batavia, U.S.A.

S. Abdullin, M. Albrow, M. Alyari, G. Apollinari, A. Apresyan, A. Apyan, S. Banerjee, L.A.T. Bauerdick, A. Beretvas, J. Berryhill, P.C. Bhat, G. Bolla[†], K. Burkett, J.N. Butler, A. Canepa, G.B. Cerati, H.W.K. Cheung, F. Chlebana, M. Cremonesi, J. Duarte, V.D. Elvira, J. Freeman, Z. Gecse, E. Gottschalk, L. Gray, D. Green, S. Grünendahl, O. Gutsche, J. Hanlon, R.M. Harris, S. Hasegawa, J. Hirschauer, Z. Hu, B. Jayatilaka, S. Jindariani, M. Johnson, U. Joshi, B. Klima, B. Kreis, S. Lammel, D. Lincoln, R. Lipton, M. Liu, T. Liu, R. Lopes De Sá, J. Lykken, K. Maeshima, N. Magini, J.M. Marraffino, D. Mason, P. McBride, P. Merkel, S. Mrenna, S. Nahn, V. O'Dell, K. Pedro, O. Prokofyev, G. Rakness, L. Ristori, B. Schneider, E. Sexton-Kennedy, A. Soha, W.J. Spalding, L. Spiegel, S. Stoynev, J. Strait, N. Strobbe, L. Taylor, S. Tkaczyk, N.V. Tran, L. Uplegger, E.W. Vaandering, C. Vernieri, M. Verzocchi, R. Vidal, M. Wang, H.A. Weber, A. Whitbeck, W. Wu

2018 JINST 13 P06015

University of Florida, Gainesville, U.S.A.

D. Acosta, P. Avery, V. Barashko, P. Bortignon, D. Bourilkov, A. Brinkerhoff, A. Carnes, M. Carver, D. Curry, R.D. Field, I.K. Furic, S.V. Gleyzer, B.M. Joshi, J. Konigsberg, A. Korytov, K. Kotov, P. Ma, A. Madorsky, K. Matchev, H. Mei, G. Mitselmakher, K. Shi, D. Sperka, N. Terentyev, L. Thomas, J. Wang, S. Wang, J. Yelton

Florida International University, Miami, U.S.A.

Y.R. Joshi, S. Linn, P. Markowitz, J.L. Rodriguez

Florida State University, Tallahassee, U.S.A.

A. Ackert, T. Adams, A. Askew, S. Hagopian, V. Hagopian, K.F. Johnson, T. Kolberg, G. Martinez, T. Perry, H. Prosper, A. Saha, A. Santra, V. Sharma, R. Yohay

Florida Institute of Technology, Melbourne, U.S.A.

M.M. Baarmand, V. Bhopatkar, S. Colafranceschi, M. Hohlmann, D. Noonan, T. Roy, F. Yumiceva

University of Illinois at Chicago (UIC), Chicago, U.S.A.

M.R. Adams, L. Apanasevich, D. Berry, R.R. Betts, R. Cavanaugh, X. Chen, O. Evdokimov, C.E. Gerber, D.A. Hangal, D.J. Hofman, K. Jung, J. Kamin, I.D. Sandoval Gonzalez, M.B. Tonjes, H. Trauger, N. Varelas, H. Wang, Z. Wu, J. Zhang

The University of Iowa, Iowa City, U.S.A.

B. Bilki[69], W. Clarida, K. Dilsiz[70], S. Durgut, R.P. Gandrajula, M. Haytmyradov, V. Khristenko, J.-P. Merlo, H. Mermerkaya[71], A. Mestvirishvili, A. Moeller, J. Nachtman, H. Ogul[72], Y. Onel, F. Ozok[73], A. Penzo, C. Snyder, E. Tiras, J. Wetzel, K. Yi

Johns Hopkins University, Baltimore, U.S.A.

B. Blumenfeld, A. Cocoros, N. Eminizer, D. Fehling, L. Feng, A.V. Gritsan, P. Maksimovic, J. Roskes, U. Sarica, M. Swartz, M. Xiao, C. You

The University of Kansas, Lawrence, U.S.A.

A. Al-bataineh, P. Baringer, A. Bean, S. Boren, J. Bowen, J. Castle, S. Khalil, A. Kropivnitskaya, D. Majumder, W. Mcbrayer, M. Murray, C. Rogan, C. Royon, S. Sanders, E. Schmitz, J.D. Tapia Takaki, Q. Wang

Kansas State University, Manhattan, U.S.A.

A. Ivanov, K. Kaadze, Y. Maravin, A. Mohammadi, L.K. Saini, N. Skhirtladze

Lawrence Livermore National Laboratory, Livermore, U.S.A.

F. Rebassoo, D. Wright

University of Maryland, College Park, U.S.A.

A. Baden, O. Baron, A. Belloni, S.C. Eno, Y. Feng, C. Ferraioli, N.J. Hadley, S. Jabeen, G.Y. Jeng, R.G. Kellogg, J. Kunkle, A.C. Mignerey, F. Ricci-Tam, Y.H. Shin, A. Skuja, S.C. Tonwar

Massachusetts Institute of Technology, Cambridge, U.S.A.

D. Abercrombie, B. Allen, V. Azzolini, R. Barbieri, A. Baty, G. Bauer, R. Bi, S. Brandt, W. Busza, I.A. Cali, M. D'Alfonso, Z. Demiragli, G. Gomez Ceballos, M. Goncharov, P. Harris, D. Hsu, M. Hu, Y. Iiyama, G.M. Innocenti, M. Klute, D. Kovalskyi, Y.-J. Lee, A. Levin, P.D. Luckey, B. Maier,

2018 JINST 13 P06015

A.C. Marini, C. Mcginn, C. Mironov, S. Narayanan, X. Niu, C. Paus, C. Roland, G. Roland, J. Salfeld-Nebgen, G.S.F. Stephans, K. Sumorok, K. Tatar, D. Velicanu, J. Wang, T.W. Wang, B. Wyslouch

University of Minnesota, Minneapolis, U.S.A.

A.C. Benvenuti, R.M. Chatterjee, A. Evans, P. Hansen, J. Hiltbrand, S. Kalafut, Y. Kubota, Z. Lesko, J. Mans, S. Nourbakhsh, N. Ruckstuhl, R. Rusack, J. Turkewitz, M.A. Wadud

University of Mississippi, Oxford, U.S.A.

J.G. Acosta, S. Oliveros

University of Nebraska-Lincoln, Lincoln, U.S.A.

E. Avdeeva, K. Bloom, D.R. Claes, C. Fangmeier, F. Golf, R. Gonzalez Suarez, R. Kamalieddin, I. Kravchenko, J. Monroy, J.E. Siado, G.R. Snow, B. Stieger

State University of New York at Buffalo, Buffalo, U.S.A.

J. Dolen, A. Godshalk, C. Harrington, I. Iashvili, D. Nguyen, A. Parker, S. Rappoccio, B. Roozbahani

Northeastern University, Boston, U.S.A.

G. Alverson, E. Barberis, C. Freer, A. Hortiangtham, A. Massironi, D.M. Morse, T. Orimoto, R. Teixeira De Lima, T. Wamorkar, B. Wang, A. Wisecarver, D. Wood

Northwestern University, Evanston, U.S.A.

S. Bhattacharya, O. Charaf, K.A. Hahn, N. Mucia, N. Odell, M.H. Schmitt, K. Sung, M. Trovato, M. Velasco

University of Notre Dame, Notre Dame, U.S.A.

R. Bucci, N. Dev, M. Hildreth, K. Hurtado Anampa, C. Jessop, D.J. Karmgard, N. Kellams, K. Lannon, W. Li, N. Loukas, N. Marinelli, F. Meng, C. Mueller, Y. Musienko[42], M. Planer, A. Reinsvold, R. Ruchti, P. Siddireddy, G. Smith, S. Taroni, M. Wayne, A. Wightman, M. Wolf, A. Woodard

The Ohio State University, Columbus, U.S.A.

J. Alimena, L. Antonelli, B. Bylsma, L.S. Durkin, S. Flowers, B. Francis, A. Hart, C. Hill, W. Ji, T.Y. Ling, B. Liu, W. Luo, B.L. Winer, H.W. Wulsin

Princeton University, Princeton, U.S.A.

S. Cooperstein, O. Driga, P. Elmer, J. Hardenbrook, P. Hebda, S. Higginbotham, A. Kalogeropoulos, D. Lange, J. Luo, D. Marlow, K. Mei, I. Ojalvo, J. Olsen, C. Palmer, P. Piroué, D. Stickland, C. Tully

University of Puerto Rico, Mayaguez, U.S.A.

S. Malik, S. Norberg

Purdue University, West Lafayette, U.S.A.

A. Barker, V.E. Barnes, S. Das, S. Folgueras, L. Gutay, M. Jones, A.W. Jung, A. Khatiwada, D.H. Miller, N. Neumeister, C.C. Peng, H. Qiu, J.F. Schulte, J. Sun, F. Wang, R. Xiao, W. Xie

Purdue University Northwest, Hammond, U.S.A.

T. Cheng, N. Parashar, J. Stupak

2018 JINST 13 P06015

Rice University, Houston, U.S.A.

Z. Chen, K.M. Ecklund, S. Freed, F.J.M. Geurts, M. Guilbaud, M. Kilpatrick, W. Li, B. Michlin, B.P. Padley, J. Roberts, J. Rorie, W. Shi, Z. Tu, J. Zabel, A. Zhang

University of Rochester, Rochester, U.S.A.

A. Bodek, P. de Barbaro, R. Demina, Y.t. Duh, T. Ferbel, M. Galanti, A. Garcia-Bellido, J. Han, O. Hindrichs, A. Khukhunaishvili, K.H. Lo, P. Tan, M. Verzetti

The Rockefeller University, New York, U.S.A.

R. Ciesielski, K. Goulianos, C. Mesropian

Rutgers, The State University of New Jersey, Piscataway, U.S.A.

A. Agapitos, J.P. Chou, Y. Gershtein, T.A. Gómez Espinosa, E. Halkiadakis, M. Heindl, E. Hughes, S. Kaplan, R. Kunnawalkam Elayavalli, S. Kyriacou, A. Lath, R. Montalvo, K. Nash, M. Osherson, H. Saka, S. Salur, S. Schnetzer, D. Sheffield, S. Somalwar, R. Stone, S. Thomas, P. Thomassen, M. Walker

University of Tennessee, Knoxville, U.S.A.

A.G. Delannoy, J. Heideman, G. Riley, K. Rose, S. Spanier, K. Thapa

Texas A&M University, College Station, U.S.A.

O. Bouhali[74], A. Castaneda Hernandez[74], A. Celik, M. Dalchenko, M. De Mattia, A. Delgado, S. Dildick, R. Eusebi, J. Gilmore, T. Huang, T. Kamon[75], R. Mueller, Y. Pakhotin, R. Patel, A. Perloff, L. Perniè, D. Rathjens, A. Safonov, A. Tatarinov, K.A. Ulmer

Texas Tech University, Lubbock, U.S.A.

N. Akchurin, J. Damgov, F. De Guio, P.R. Dudero, J. Faulkner, E. Gurpinar, S. Kunori, K. Lamichhane, S.W. Lee, T. Mengke, S. Muthumuni, T. Peltola, S. Undleeb, I. Volobouev, Z. Wang

Vanderbilt University, Nashville, U.S.A.

S. Greene, A. Gurrola, R. Janjam, W. Johns, C. Maguire, A. Melo, H. Ni, K. Padeken, P. Sheldon, S. Tuo, J. Velkovska, Q. Xu

University of Virginia, Charlottesville, U.S.A.

M.W. Arenton, P. Barria, B. Cox, R. Hirosky, M. Joyce, A. Ledovskoy, H. Li, C. Neu, T. Sinthuprasith, Y. Wang, E. Wolfe, F. Xia

Wayne State University, Detroit, U.S.A.

A. Gutierrez, R. Harr, P.E. Karchin, N. Poudyal, J. Sturdy, P. Thapa, S. Zaleski

University of Wisconsin - Madison, Madison, WI, U.S.A.

M. Brodski, J. Buchanan, C. Caillol, D. Carlsmith, S. Dasu, L. Dodd, S. Duric, B. Gomber, M. Grothe, M. Herndon, A. Hervé, U. Hussain, P. Klabbers, A. Lanaro, A. Levine, K. Long, R. Loveless, V. Rekovic, T. Ruggles, A. Savin, N. Smith, W.H. Smith, N. Woods

†: Deceased

1: Also at Vienna University of Technology, Vienna, Austria

2: Also at IRFU; CEA; Université Paris-Saclay, Gif-sur-Yvette, France

2018 JINST 13 P06015

3: Also at Universidade Estadual de Campinas, Campinas, Brazil
4: Also at Federal University of Rio Grande do Sul, Porto Alegre, Brazil
5: Also at Université Libre de Bruxelles, Bruxelles, Belgium
6: Also at Institute for Theoretical and Experimental Physics, Moscow, Russia
7: Also at Joint Institute for Nuclear Research, Dubna, Russia
8: Also at Cairo University, Cairo, Egypt
9: Also at Suez University, Suez, Egypt
10: Now at British University in Egypt, Cairo, Egypt
11: Also at Zewail City of Science and Technology, Zewail, Egypt
12: Also at Department of Physics; King Abdulaziz University, Jeddah, Saudi Arabia
13: Also at Université de Haute Alsace, Mulhouse, France
14: Also at Skobeltsyn Institute of Nuclear Physics; Lomonosov Moscow State University, Moscow, Russia
15: Also at Tbilisi State University, Tbilisi, Georgia
16: Also at Ilia State University, Tbilisi, Georgia
17: Also at CERN; European Organization for Nuclear Research, Geneva, Switzerland
18: Also at RWTH Aachen University; III. Physikalisches Institut A, Aachen, Germany
19: Also at University of Hamburg, Hamburg, Germany
20: Also at Brandenburg University of Technology, Cottbus, Germany
21: Also at MTA-ELTE Lendület CMS Particle and Nuclear Physics Group; Eötvös Loránd University, Budapest, Hungary
22: Also at Institute of Nuclear Research ATOMKI, Debrecen, Hungary
23: Also at Institute of Physics; University of Debrecen, Debrecen, Hungary
24: Also at Indian Institute of Technology Bhubaneswar, Bhubaneswar, India
25: Also at Institute of Physics, Bhubaneswar, India
26: Also at Shoolini University, Solan, India
27: Also at University of Visva-Bharati, Santiniketan, India
28: Also at University of Ruhuna, Matara, Sri Lanka
29: Also at Isfahan University of Technology, Isfahan, Iran
30: Also at Yazd University, Yazd, Iran
31: Also at Plasma Physics Research Center; Science and Research Branch; Islamic Azad University, Tehran, Iran
32: Also at Università degli Studi di Siena, Siena, Italy
33: Also at ENEA - Casaccia Research Center, S. Maria di Galeria, Italy
34: Also at Facoltà Ingegneria; Università di Roma, Roma, Italy
35: Also at INFN Sezione di Milano-Bicocca (a; Università di Milano-Bicocca, Milano, Italy
36: Also at Laboratori Nazionali di Legnaro dell'INFN, Legnaro, Italy
37: Also at Purdue University, West Lafayette, U.S.A.
38: Also at International Islamic University of Malaysia, Kuala Lumpur, Malaysia
39: Also at Malaysian Nuclear Agency; MOSTI, Kajang, Malaysia
40: Also at Consejo Nacional de Ciencia y Tecnología, Mexico city, Mexico
41: Also at Warsaw University of Technology; Institute of Electronic Systems, Warsaw, Poland
42: Also at Institute for Nuclear Research, Moscow, Russia
43: Now at National Research Nuclear University 'Moscow Engineering Physics Institute' (MEPhI), Moscow, Russia
44: Also at St. Petersburg State Polytechnical University, St. Petersburg, Russia
45: Also at University of Florida, Gainesville, U.S.A.
46: Also at Budker Institute of Nuclear Physics, Novosibirsk, Russia
47: Also at Faculty of Physics; University of Belgrade, Belgrade, Serbia

2018 JINST 13 P06015

48: Also at University of Belgrade; Faculty of Physics and Vinca Institute of Nuclear Sciences, Belgrade, Serbia
49: Also at Scuola Normale e Sezione dell'INFN, Pisa, Italy
50: Also at National and Kapodistrian University of Athens, Athens, Greece
51: Also at Riga Technical University, Riga, Latvia
52: Also at Universität Zürich, Zurich, Switzerland
53: Also at Stefan Meyer Institute for Subatomic Physics (SMI), Vienna, Austria
54: Also at Gaziosmanpasa University, Tokat, Turkey
55: Also at Adiyaman University, Adiyaman, Turkey
56: Also at Istanbul Aydin University, Istanbul, Turkey
57: Also at Mersin University, Mersin, Turkey
58: Also at Piri Reis University, Istanbul, Turkey
59: Also at Izmir Institute of Technology, Izmir, Turkey
60: Also at Necmettin Erbakan University, Konya, Turkey
61: Also at Marmara University, Istanbul, Turkey
62: Also at Kafkas University, Kars, Turkey
63: Also at Istanbul Bilgi University, Istanbul, Turkey
64: Also at Rutherford Appleton Laboratory, Didcot, United Kingdom
65: Also at School of Physics and Astronomy; University of Southampton, Southampton, United Kingdom
66: Also at Monash University; Faculty of Science, Clayton, Australia
67: Also at Instituto de Astrofísica de Canarias, La Laguna, Spain
68: Also at Utah Valley University, Orem, U.S.A.
69: Also at Beykent University, Istanbul, Turkey
70: Also at Bingol University, Bingol, Turkey
71: Also at Erzincan University, Erzincan, Turkey
72: Also at Sinop University, Sinop, Turkey
73: Also at Mimar Sinan University; Istanbul, Istanbul, Turkey
74: Also at Texas A&M University at Qatar, Doha, Qatar
75: Also at Kyungpook National University, Daegu, Korea

2018 JINST 13 P06015